AGU PUBLICATIONS

JGR

Journal of Geophysical Research: Solid Earth

RESEARCH ARTICLE
10.1002/2017JB015004

Key Points:
- Application of waveform inversion techniques on seismic data provided high-quality velocity images of zero-age, upper oceanic crust at the East Pacific Rise
- The imaged low-velocity anomalies are associated with the presence of upgoing and downgoing hydrothermal pathways within the axial plane of the fast-spreading ridge
- The presence of high thermal regime and crustal permeability acts in symbiosis and is equally important for driving vigorous hydrothermal flow along the ridge axis

Supporting Information:
- Supporting Information S1

Correspondence to:
M. Marjanović,
marjanovic@ipgp.fr

Citation:
Marjanović, M., Fuji, N., Singh, S. C., Belahi, T., & Escartín, J. (2017). Seismic signatures of hydrothermal pathways along the East Pacific Rise between 9°16′ and 9°56′N. *Journal of Geophysical Research: Solid Earth*, *122*, 10,241–10,262. https://doi.org/10.1002/2017JB015004

Received 19 SEP 2017
Accepted 20 NOV 2017
Accepted article online 24 NOV 2017
Published online 18 DEC 2017

Seismic Signatures of Hydrothermal Pathways Along the East Pacific Rise Between 9°16′ and 9°56′N

Milena Marjanović[1], Nobuaki Fuji[1], Satish C. Singh[1], Thomas Belahi[1,2], and Javier Escartín[1]

[1]Equipe de Géosciences Marines, Institut de Physique du Globe de Paris, Paris, France, [2]Now at Sia Partners, Paris, France

Abstract We apply wave equation-based techniques to 2-D seismic data to characterize the nature of zero-age upper crust at the East Pacific Rise from 9°16′ to 9°56′N. The final velocity model reveals a number of low-velocity anomalies, complex in shape, extending down to ~1 km below the seafloor. We attribute them to the presence of hydrothermal flow. Depending on their spatial correlation with the previously identified tectonic discontinuities in bathymetry and presence of venting, we classify them as downgoing and upgoing pathways, respectively. This distinction is not always clear; within the third-order discontinuities at 9°20′ and 9°37′N, both pathways may be present. The region north of 9°44′N, known for its magmatic robustness and volcanic activity, is represented by five low-velocity perturbations. Three of these anomalies are spatially correlated with the fourth-order discontinuities and attributed to the presence of the on-axis recharge zones. The remaining two anomalies underlie two vent clusters, marked as hydrothermally active sites after the last documented eruption event. These velocity anomalies can be thus identified as the up-flow pathways or at least their remnants. By comparing our results to the available interdisciplinary data sets, we show that the interaction between the tectono-magmatic and hydrothermal processes is not straightforward due to different timescales at which they operate. However, for developing, maintaining, and driving vigorous, high-temperature hydrothermal flow, the high crustal permeability and high thermal regime must coexist in time and space.

1. Introduction

Since the first hydrothermal vent system was identified along the Galapagos spreading center in the late 1970s (Corliss et al., 1979), the number of discovered vent fields has increased exponentially (e.g., Baker et al., 2016; Baker & German, 2004; Baker et al., 1995; Beaulieu et al., 2013, 2015; Hannington et al., 2004). Nowadays, the discharge zones of hydrothermal fluids are known to be ubiquitously present along the mid-ocean ridge (MOR) system, at all spreading rates and within a wide variety of geological settings (e.g., Baker et al., 2016; Baker & German, 2004; Cannat et al., 2004; Wilcock & Delaney, 1996). Regardless of the geological environment within which the hydrothermal circulation is taking place, the two main governing factors of hydrothermal circulation are believed to be common: high thermal regime and high crustal permeability. However, which one predominates is not well understood.

At fast to intermediate spreading centers the prevailing heat source for establishing hydrothermal circulation is represented by frequently replenished intracrustal reservoirs of melt (Baker, 2009), that is, axial magma lenses (AMLs). The AMLs have been imaged in seismic data (e.g., Blacic et al., 2004; Carbotte et al., 2006, 2013, 2000; Detrick et al., 1987, 1993, 2002; Hooft et al., 1997; Jacobs et al., 2007; Marjanović et al., 2014; Vera et al., 1990), some portions of which were inferred to be highly molten (e.g., Canales et al., 2006; Collier & Singh, 1997; Marjanović et al., 2015; Singh et al., 1998; Xu et al., 2014). Although some of the studies argued for spatial correlation between melt-rich AML and incidence of vigorous venting (Canales et al., 2006; Singh et al., 1999), more extensive MOR-wide study showed no consistent relationship (Baker, 2009).

While identified vent orifices provide a good hint about the location of the upgoing pathways of discharging fluid, little is known whereabouts the seawater penetrates the crust and establishes the downgoing pathway. High permeability zones, generally represented by faults, and/or zones of interconnected cracks and fissures that hydrothermal fluids use as pathways for circulating within the crust, are challenging for seismic imaging and have not been mapped in seismic data collected at fast-spreading centers.

One of the best places to study hydrothermal systems along the MORs is the East Pacific Rise (EPR) 9°50′N. Early visual and acoustic imaging of the seafloor (Haymon et al., 1991) and plume mapping (Baker et al.,

1994) showed the presence of hydrothermal vents concentrated within 9°50′N region. It was also within this area that a complete volcanic cycle was documented, demarcated by two submarine volcanic eruptions that happened in 1991–1992 (Haymon et al., 1993; Rubin et al., 1994) and 2005–2006 (Tolstoy et al., 2006), witnessing high magma budget in the EPR's lithosphere. This dynamic portion of the MOR system was also a focus site for full suite of continuous and interconnected studies focused on topics ranging from "magma to microbe" (Fornari et al., 2012). They included examination of biological communities, volcanic, magmatic, tectonic and hydrothermal activity, and their chemical imprints on the rocks and fluids expelled within the region (e.g., Fornari et al., 2012; Goss et al., 2010; Kelley et al., 2002; Lutz et al., 2008; Nooner et al., 2014; Soule et al., 2007; Tolstoy et al., 2008; Toomey et al., 2007; Von Damm, 2004; Von Damm & Lilley, 2004; White et al., 2006; Yücel & Luther, 2013).

In 2008, a multichannel seismic (MCS) survey, including the collection of the along-axis swath, was conducted in this area (e.g., Mutter et al., 2009). The analysis of the along-axis data indicated the presence of a fine-scale AML segmentation linked to the seafloor morphology (Carbotte et al., 2013, 2015). In addition, it has been shown that some of the AML segments are highly molten (Marjanović et al., 2015; Xu et al., 2014). To further explore and characterize zero-age upper crust along the EPR, we apply elastic 2-D wave-equation based techniques (wave equation tomography and waveform inversion) to redatumed axis-centered seismic profile spanning the region between ~9°16′ and 9°56′N. The redatuming technique (Harding et al., 2007) was first extensively tested on synthetic data sets and then applied to real data. These data were then subject to a wave equation-based tomography to obtain information on large-scale to midscale velocity variations. This result also provides a starting velocity model that is used as an input to the elastic waveform inversion for further estimation of fine-scale velocity changes. Several low-velocity anomalies are identified within the 2-D velocity model, with the most complex ones located within the eruption area. Their distribution suggests that at least one part of the hydrothermal circulation is taking place along the ridge axis plane.

2. Background

2.1. Geological Setting

Our study area encompasses a portion of the EPR that extends between the Siqueiros Transform Fault (TF) in the south and the Clipperton TF in the north (Figure 1a), which has been the focus of many interdisciplinary studies since the early stage of the MOR exploration (Herron et al., 1978, 1980; Menard, 1960; Orcutt et al., 1976). This segment of the ridge axis is further divided into two second-order segments, the southern and northern one, separated by a prominent Overlapping Spreading Center (OSC) at 9°03′N, where the two limbs of the EPR are offset by 8 km, and overlapped by 27 km (Sempere & Macdonald, 1986). In addition to this second-order OSC, within the present-day EPR axis zone, both side-scan sonar data (Macdonald et al., 1992) and recent high-resolution bathymetric mapping of the seafloor (White et al., 2006) identified additional but smaller OSCs or third-order discontinuities. Within these third-order segments, smaller changes in ridge axis orientation and/or changes in the character of the axial summit through (AST) are also observed (Carbotte et al., 2013, 2015; White et al., 2006). They are defined as fourth-order discontinuities with a life span of about several hundreds to thousand years (Carbotte et al., 2013; Langmuir et al., 1986; Macdonald et al., 1988; White et al., 2002, 2006). Spatially, these finer-scale (third- and fourth-order) morphotectonic discontinuities are well correlated with the prominent changes in the recorded reflection signal from the AML, that is, fine-scale magmatic segmentation, which suggests their genetic relationship (Carbotte et al., 2013, 2015; Kent et al., 1993). The area extending between 9°46′ and 9°56′N, underlain by three well-defined AML segments (Carbotte et al., 2013), coincides with the region of two documented eruptions in 1991–1992 (Haymon et al., 1993) and 2005–2006 (Figure 1b) (Tolstoy et al., 2006). It represents one of the most volcanically active zones along the MOR system, if we exclude the portions of direct ridge-hot spot interaction, for example, Axial Segment along the Juan de Fuca Ridge, influenced by the Cobb hot spot (e.g., Chadwick et al., 2005; Wilcock et al., 2016). In addition, an abundance of hydrothermal venting activity has been taking place in this area (Figure 1b) (Fornari et al., 2004, 2012; Haymon et al., 1991; Haymon & White, 2004; Sohn et al., 1998, 1999). Different types of hydrothermal discharge zones were identified (e.g., Fornari et al., 2004; Haymon et al., 1991, 1993; Von Damm, 2000). Along the floor of the AST or along the AST's walls number of high-temperature vents/vent clusters (including black, gray and white smokers) has been mapped. In addition, these high-temperature, focused vent sites are almost always accompanied by a number of diffuse flow sites created by shallow subsurface seawater circulation with a mildly heated (up to 100°C) emanating fluids

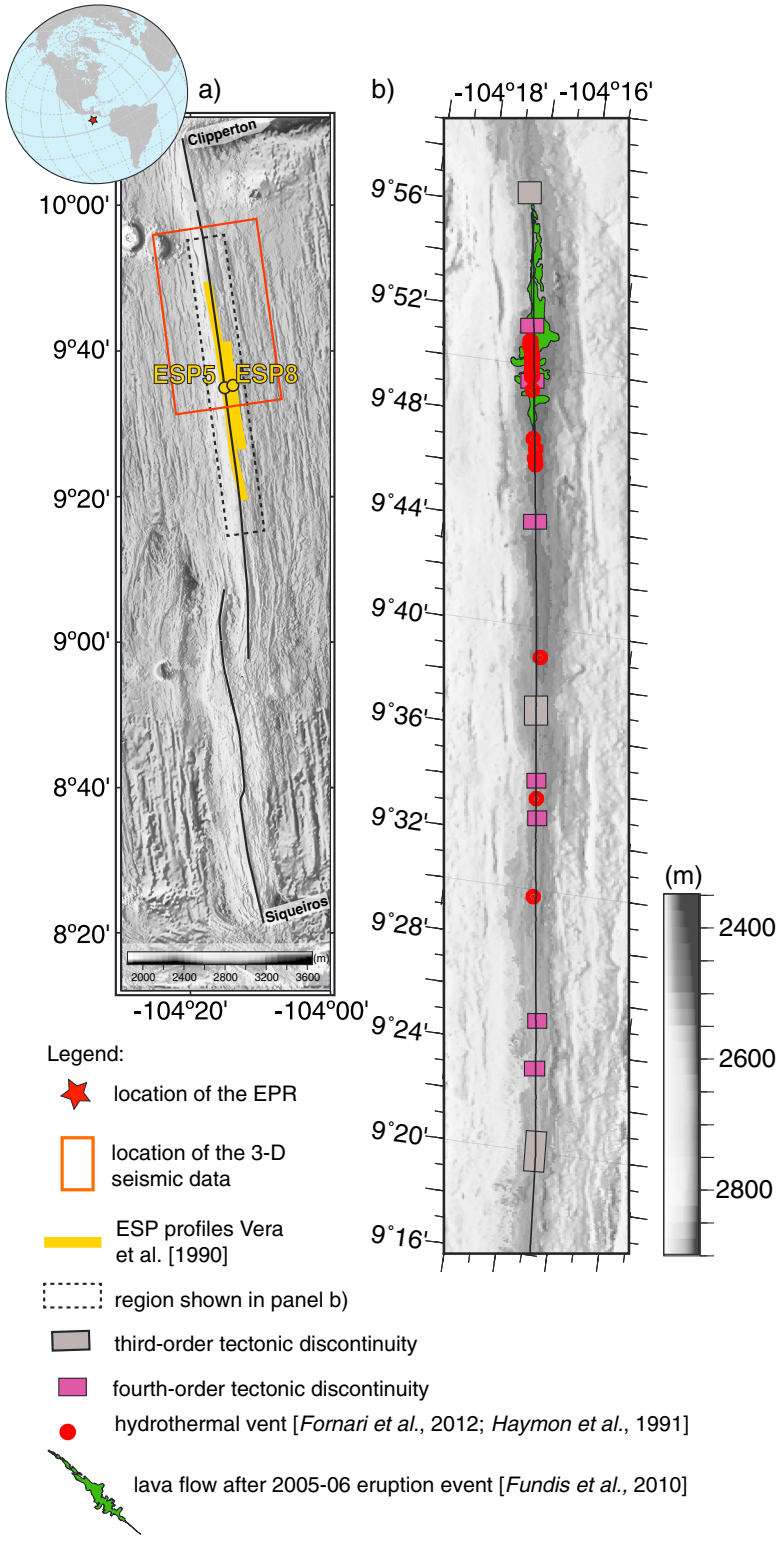

Figure 1. Location of seismic lines acquired during the MGL0812 expedition aboard R/V *M. G. Langseth*. (a) The regional, gray-shaded seafloor bathymetry map with the globe inset is a composite map derived from the global multiresolution topography database (Ryan et al., 2009) and multibeam sonar data acquired during the cruise (gridded at 50 m); the Siqueiros and Clipperton transform faults, and the OSC at 9°03′N are indicated. (b) The multibeam sonar data are used for the local map, encompassing the extent of the 2-D seismic line (portion of the axis2r1) used in this study. The remaining symbols are indicated in the legend.

(Bemis et al., 2012; Delaney et al., 1992; Rona & Tivett, 1992; Schultz et al., 1992; Von Damm & Lilley, 2004). It has been shown that the temperature and chemistry of the egressing fluid vary significantly between the neighboring chimneys (e.g., Fornari et al., 2004; Scheirer et al., 2006; Von Damm, 2000, 2004). Furthermore, fluid properties emanated from a single chimney may vary through time: new vents can appear, and the existing ones disappear, due to magmatic cycling. For instance, following the 2005–2006 eruption, several high-temperature vents became extinct (M, Q, Choo Choo, and Tubeworm Pillar) and new vents sites appeared (Hobbit Hole, Tamtown, Crab Spa, etc.) (Fornari et al., 2012; Von Damm, 2006). During the posteruption dives, the activity of two clusters centered at ~9°47′N and 9°50.3′N was examined with the hydrothermal activity within the northern one being more prominent. The inventory of all known active vent sites after the last documented eruption is provided in Table S1 in the supporting information. A more recent study, conducted in 2011 using continuous tows of sensors sensitive to hydrothermal tracers (Baker et al., 2016), portrays the most complete representation available of the recent hydrothermal activity along the EPR. This study, conducted 3 years after the eruption event, shows that the vigorous hydrothermal discharge has been established between ~9°37′N and 9°44′N, with a small gap (~2 km) between 9°41′ and 42′N. In addition, it shows no presence of venting within the region extending between 9°44′ and 9°48′, which was active within the posteruption setting and was represented by the vent cluster centered at 9°47′N (Fornari et al., 2012; Von Damm, 2006). In contrast, the cluster centered at 9°50.3′N still exhibits the most prominent high-temperature hydrothermal activity. The observed differences in hydrothermal activity depicted in earlier studies (e.g., Fornari et al., 2012; Haymon et al., 1991) and recent detailed observations (Baker et al., 2016) can be explained by temporal variation and constant changes in the dynamics of the along-axis hydrothermal system(s); they can also be the result of scarcity in sampling of the hydrothermal activity by the earlier studies.

Along with the discovery of the vents, the most incredible forms of life have been revealed, including tube warm communities, colonies of clams, crabs, gastropods, and variety of microorganisms (Kelley et al., 2002; Shank et al., 1998), and may tell us a story of the onset of life (Weiss et al., 2016). Their existence is highly controlled by volcanic and hydrothermal habitats at MOR within which they thrive.

2.2. Hydrothermal Circulation From Numerical Modeling and Microseismicity

Most of our knowledge on hydrothermal circulation along spreading centers is based on analytical and numerical modeling studies (Coumou et al., 2006; Coumou, Driesner, Geiger, et al., 2009; Coumou, Driesner, Weis, et al., 2009; Coumou et al., 2008; Fontaine et al., 2011, 2014; Germanovich et al., 2000; Hasenclever et al., 2014; Liu & Lowell, 2009; Lowell & Germanovich, 1994; Lowell & Yao, 2002; Lowell et al., 2013; Rosenberg et al., 1993; Schoofs & Hansen, 2000; Wilcock, 1998). A majority of these models used the EPR as a prototype due to the availability of interconnected, interdisciplinary studies and known hydrothermal activity. Initially, based on the available thermal and geochemical models (Dunn et al., 2000; Johnson et al., 1993; Lowell & Yao, 2002), ridge-parallel inward facing faults in the vicinity of the ridge axis were proposed as the ideal environments for seawater to enter the crust and establish cross axis loop of hydrothermal circulation (e.g., Bonatti, 1975; Kelley et al., 2002; Lister, 1977; Lowell et al., 1995; Wolery & Sleep, 1976). However, the microearthquakes recorded in 2003–2004 revealed a zone of thermal cracking in a vertical, pipe-like cluster on the ridge axis, interpreted as a downgoing pathway for the hydrothermal circulation (Tolstoy et al., 2008; Waldhauser & Tolstoy, 2011). This observation indicated that the fluid recharge zone is located at the ridge axis and that the hydrothermal circulation cell is aligned with the ridge axial plane. Based on a 3-D numerical simulation study, Coumou et al. (2008) suggested that convection cells are organized into up-flow channels directly beneath vents orifices surrounded by narrow zones of focused and relatively warm downflow. A recent high-resolution, 3-D whole-crustal modeling study proposed the existence of a shallow on-axis and deep off-axis flows that merge above the AML, to build vent sites on the ridge axis (Hasenclever et al., 2014).

3. Methods

3.1. Data Acquisition

During R/V *Marcus G. Langseth* expedition MGL0812 conducted in 2008, a swath of seismic reflection data spanning the innermost portion of the EPR axis from the Siqueiros to Clipperton TF was acquired (Figure 1a). The data were recorded using four 6 km long solid streamers, each containing 468 channels

spaced at 12.5 m. The seismic source was produced by two tuned air gun arrays spaced at 75 m. Each of the air gun strings contained nine air guns, with a total volume of 1,650 in^3, firing at a 75 m space interval. The arrays were firing in an alternating mode, which for a given four-streamer geometry resulted in a swath of seismic data composed of eight 2-D seismic lines spaced at 37.5 m. For the 2-D inversion work, we extract shot lines from line axis2r1 (Figure 1b) recorded along the streamer 2 (Figure S2), which samples the innermost zone of the AST (Carbotte et al., 2013; Marjanović et al., 2015). Moreover, the data recorded along this streamer exhibit the highest signal-to-noise ratio (Marjanović et al., 2015). By using composite line recorded along a single cable in alternating shooting mode, we reduce the shot interval to 37.5 m. For the axis2r1, the gun array was deployed at 7.5 m depth, so were the receivers along the streamer. Details considering particular effects of the acquisition geometry on waveform modeling are provided in section 3.2.2.

We limit the region of our study between ~9°16′ and 9°56′N (Figure 1b). The southern boundary, 9°16′N, is chosen as the northernmost limit of the 9°03′ OSC, which represents the zone of important topographic variations. The northern boundary is defined at 9°56′N as the location of a change in orientation of the along-axis seismic line for about 4° in the counterclockwise sense (Figure 1a).

3.2. Data Processing

3.2.1. Seismic Data Processing

We follow the seismic data processing approach of Aghaei et al. (2014), which was previously tested on the EPR data set collected across the ridge axis during the MGL0812 survey (Aghaei, 2013). We first apply a bandpass filter with cutoff frequencies 1–6–200–220 Hz to denoise the data and conduct trace editing to exclude bad channels; the edited channels are reconstructed by interpolation. Furthermore, we also reconstruct a few missing shots by interpolation of the neighboring shots. The interpolation procedure is valid on the assumption that there is no important variation in the seafloor, which was checked for all the regions for which the recreation of the shots was required. The next step included the application of a 2-D filter using the *Lift* techniques developed by Choo et al. (2004). The Lift approach is based on subdividing the data into frequency bands and then applying a series of filters. The tests showed that the dominant noise for the EPR data lies below 15 Hz (Aghaei, 2013). Thus, the data were subdivided into low- (0–14–16 Hz), middle- (14–16–20–25 Hz), and high- (20–25–200–220 Hz) frequency bands. An F-K filter is applied in the low-frequency band within the Lift. In addition, we apply a surface consistent amplitude balancing that accounts for weak channels that are not results of geology and low-pass filter with a corner frequency of 25–30 Hz. After filtering, we apply top (~1 s above the seafloor) and bottom (at 6 s) mutes. The data are also tapered both in the time and offset domain using a Tukey window taper to minimize edge effects for extrapolation that follows.

To account for the difference between the real 3-D data and generated 2-D synthetic in the forward modeling stage, in the inversion process we also apply *3-D to 2-D correction* (Pica et al., 1990). This correction consists of amplitude scaling by $\sqrt{t}$ and convolution of the data by $1/\sqrt{t}$. We apply these corrections prior to extrapolation process for two reasons: (1) we use 2-D Green function for extrapolation (i.e., 2-D is assumed) and (2) as almost the entire water column (3.2 s) is eliminated, the scaling factor as a function of time is different in the extrapolated data.

3.2.2. Kirchhoff Wave Equation Redatuming

Wave equation redatuming is defined as upward or downward continuation of the seismic data when redefining reference surface on which shots and receivers are located (Berryhill, 1979). In the literature, different terminology has been used to describe it: downward continuation (Ghosal et al., 2014; Wang et al., 2014; Yilmaz, 2001), wave equation extrapolation (Shtivelman & Canning, 1988), Synthetic Ocean Bottom Experiment (Arnulf et al., 2011; Harding et al., 2007; Henig et al., 2012), or wave equation datuming (Berryhill, 1979, 1984). Hereinafter, we will refer to the method as wave equation redatuming. In the past several years, the wave equation redatuming came into focus as the need to better understand deep marine subsurface (Arnulf et al., 2011, 2012; Arnulf, Harding, Kent, et al., 2014; Arnulf, Harding, Singh, et al., 2014; Ghosal et al., 2014; Harding et al., 2007; Henig et al., 2012; Wang et al., 2014). There are several reasons behind the application of the wave equation redatuming on the data set collected along the EPR. First, it facilitates the inversion process by not only collapsing seafloor diffractions and thus improving the imaging quality but also bringing refraction arrivals to near virtual source-receiver offsets, in order to deepen sensitivity (Arnulf et al., 2011). Second, by removing most of the water column from the calculation we reduce the computational time by approximately 50%.

For the EPR along-axis data redatuming, we use standard 2-D time domain Kirchhoff integral approach in two passes (Berryhill, 1979, 1984; Harding et al., 2007). Within the first pass the receiver wavefields for all shot gathers are redatumed from 7.5 m below sea surface (nominal receivers depth) to ~2,394 m (or 3.2 s) below the sea surface, that is, an arbitrary surface close to the almost flat seafloor, which we define as a redatuming depth (Figure S1). However, during the first pass of wave equation redatuming application, some geometry manipulation is needed due to particular survey geometry of the chosen seismic line (i.e., a 2-D line extracted from 3-D acquisition setting). The data used in this study combine records from a single streamer (here streamer 2) that was 75 m away from the ship's axis to its starboard side (Figure S2). The alternating gun arrays and position of the streamer 2 resulted in different source-receiver distance for odd shot numbers (203.5 m for the nearest offset) and source-receiver distance for even shot numbers (229.5 m for the nearest offset). These differences in odd and even shot locations could potentially produce artifacts when the shots are combined in the redatumed data. To overcome the problem and make use of all recorded shots, within the first pass we redatum even and odd shot gathers separately using the same redatuming parameter that defines a horizontal distance between a given source and nearest virtual receiver, here 200 m. As a result all redatumed shot gathers follow the same geometry, and the shot spacing is kept at 37.5 m. It has to be mention that the described approach is valid upon the assumption of negligible topography variation across the ridge axis for half of the given air gun arrays separation (i.e., 37.5 m). After the first pass and prior to resorting the data into receiver gathers, we apply a band-pass filter (4–6–20–25 Hz). This is followed by the second pass within which shot wavefields for all virtual receiver gathers are redatumed to the redatuming depth level without any geometry modifications (Figure S1b). Finally, we resample the data from 2 ms to 1 ms sampling rate (required by the inversion scheme), with the application of antialiasing filter, and resort the data into shot gathers.

3.2.3. Synthetic Tests on Wave Equation Redatuming

Previous studies using the wave equation redatuming technique (e.g., Arnulf et al., 2011; Ghosal et al., 2014; Wang et al., 2014) pointed out that far offsets in the extrapolated data were unreliable and hence were not used in the inversion. However, their estimate of the offset limits was ad hoc. In order to quantitatively define source-receiver offset limits, we conducted a synthetic test using a 1-D velocity model from Vera et al. (1990). First, we compute synthetic shot gathers using the 1-D expanded spread profile (ESP) velocity function, ESP5, mimicking the MGL0812 survey geometry (including the modeled source addressed in section 3.3.4). We then perform wave equation redatuming, following the same steps as for the real EPR data set (Figure 2a), excluding some sophisticated data processing steps such as Lift. Second, we compute synthetic shot gathers for source and receiver arrays at a depth of 2,394 m (Figure 2b). We quantitatively compare traces from these synthetic tests and conclude that for the given velocity model only the data ranging between ~2 and 4 km offset. Within this offset range, which we use for further analyses, the phase and amplitudes of the first arrival match well, and there are no artifacts introduced by the application of the wave equation redatuming (Figure 2c).

3.3. Wave Equation Inversion-Based Techniques

The wave equation inversion techniques applied here are wave equation tomography and waveform inversion, both of which use the same modeling algorithm, a staggered grid elastic finite-difference scheme (fourth order in space and second order in time) in time domain (Levander, 1988; Shipp & Singh, 2002). The algorithm aims at minimizing the misfit function, defined as the difference between real and synthetic data. While the wave equation tomography method provides intermediate to long wavelength information (the first Fresnel zone is typically equal or greater than three dominant wavelengths), the waveform inversion provides finer-scale velocity information (Wang et al., 2014).

3.3.1. Wave Equation Tomography

The most traditional approach for obtaining starting velocity model for 2-D waveform inversion has been through ray-based traveltime tomography that retrieves compressional wave velocity model by inverting first-arrival traveltimes (e.g., Arnulf et al., 2012; Brenders & Pratt, 2007; Ghosal et al., 2014; Pratt & Goulty, 1991; Shipp & Singh, 2002; Treister & Huber, 2016). However, there are several limitations of the ray traveltime tomography approach. First, ray theory cannot account geology for complex finite-frequency wave propagation and complicated geological structures. Also, it does not provide good constraints on low-velocity zones as transmitted waves are deflected from it and thus preferentially sampling surrounding high-velocity zone (Vasco et al., 1995). Furthermore, it relies on a high-frequency approximation and ignores finite-frequency Fresnel zone (Tromp et al., 2005). It also assumes that the source wavelet is not distorted and seismic events

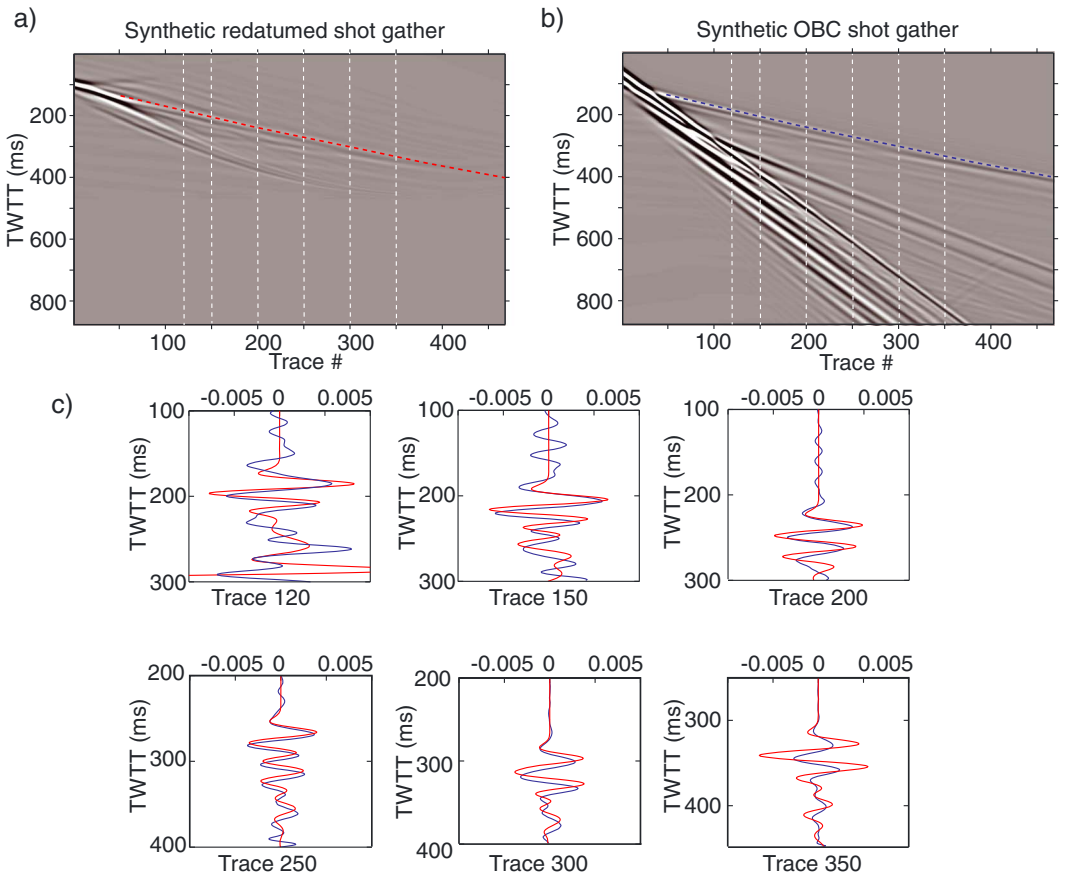

Figure 2. Shot gathers extracted from 2-D synthetic seismic lines that: (a) mimic the survey geometry of the MGL0812 experiment with applied wave equation redatuming; the first refraction arrival is marked in red dashed line; (b) synthetic ocean bottom cable (OBC) survey, that is, use the survey geometry as if the data were collected at the redatumed level; the first refraction arrival is indicated in dashed blue line. (c) Traces extracted from the synthetic shot gathers shown in Figures 2a (in red) and 2b (in blue), spanning different source-receiver offsets. Locations of the traces shown in each panel are marked in the corresponding shot gathers in dashed white lines.

are completely characterized by traveltimes, conditions that commonly are not met (Woodward, 1992). Furthermore, one requires the picking of arrival times, which can be time consuming and tedious. To overcome the above issues, a wave equation based tomography was proposed (Luo & Schuster, 1991; Woodward, 1992). Here we use the implementation of Wang et al. (2014). In the wave equation tomography, the synthetic data are cross correlated with real data, providing appropriate delay time between observed and synthetic data within the previously identified window. We run wave equation tomography on carefully extracted refracted arrival from redatumed shots to retrieve long and middle wavelength structures and obtain best-possible starting velocity model for waveform inversion that can alleviate the cycle-skipping problem (synthetic phases arrive within half of dominant frequency of the observed phases) and assure convergence to a global minimum. It has to be mentioned that although the wave equation tomography does not require cumbersome traveltime picking, for the EPR data the window has to be defined and tailored to encompass the first refraction arrival and preferably exclude all other events.

3.3.2. Waveform Inversion

With the exponential increase in computational power, the collection of longer offset and lower frequency data sets, the interest in conducting waveform inversion has augmented since the theoretical foundations of the method were laid out (Lailly, 1983; Mora, 1987; Tarantola, 1984; 1986). A review and an extensive bibliography on different approaches to the inverse problem are provided by Virieux and Operto (2009) and will not be discussed further.

Here we use gradient method (Levander, 1988; Shipp & Singh, 2002) by cross correlating the forward wavefield and back-propagated wavefield residual from virtual receivers. We start with a model obtained from

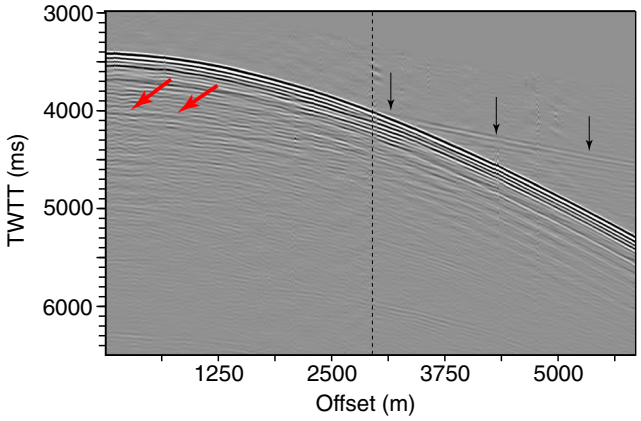

Figure 3. Shot gather extracted from the 2-D seismic line at ~9°53′N after applying processing flow outlined in the text. Black arrows show first refraction event; dashed vertical line shows the offset at which the refraction event emerges (~2,975 m); red arrows mark the presence of the AML reflector.

wave equation tomography and define residual data (misfit) as the difference between the observed and synthetic data using given velocity model. A step length is found by minimizing the misfit based on gradient direction (Pica et al., 1990). To minimize computational cost, we use conjugate gradient rather than the steepest descent. The process is repeated until the misfit function reaches some constant value (the variation between iterations is less than 1%) and residuals are reduced.

3.3.3. Model(s) Parameterization

The two wave equation-based inversion approaches share the same geometry for the inversion. The size of the model is 6,818 × 333 grid points starting from the redatumed level. The grid spacing is 12.5 m (in horizontal distance and depth), and time step increment is 1 ms. The absorbing surface boundaries are used within the models. On both sides of the models, ~6 km is padded to account for the edge effects. For the inversion 490 shots, with 150 m shot spacing, are used to reduce computational cost. We do not invert for shear velocity (Vs) and density, but rather derive them from compressional velocity (Vp) using relationships from Castagna et al. (1985) and Fliedner et al., (1998), and Gardner et al., (1974), respectively. For the wave equation tomography, we test three different Vp starting models obtained from different 1-D ESP profiles (Vera et al., 1990) (Figure S3a) extended to 2-D. We examine smoothed (1) a 1-D ESP5 model function obtained at 9°34.4′N on the ridge axis; (2) a 1-D ESP8 obtained at point location 9°35′N at ~2.5 km east of the ridge axis; and (3) a 1-D velocity function that combines the two above. A 375 m (horizontal) and 62.5 m (vertical) Gaussian smoothing for calculating gradient is applied to obtain smooth final velocity model after 99 iterations. Our preferred final wave equation tomography model is used as the starting model for the waveform inversion. During the waveform inversion we reduce the horizontal smoothing to 125 m. While the wave equation tomography inversion is performed within the predefined window designed to encompass refraction arrival, for the waveform inversion we extend the window for additional 200 ms.

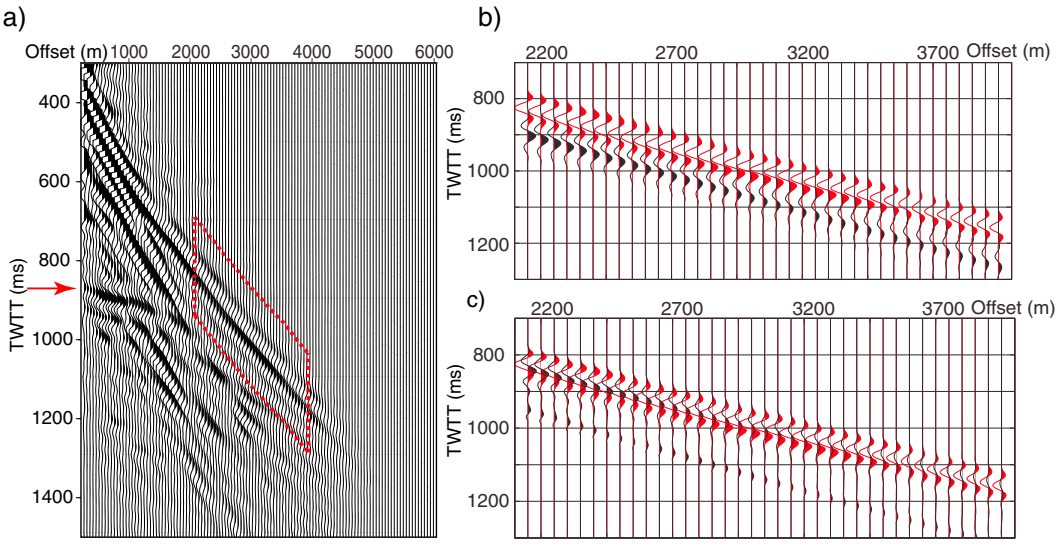

Figure 4. (a) Shot gather shown in Figure 3 after application of wave equation redatuming. For better visibility, every twentieth trace is displayed. The red arrow marks the presence of the AML reflection at near offset; the dashed rhomboid indicates the window within which cross correlation between observed and calculated data is done during wave equation tomography. Comparison of observed data (in red) and synthetically calculated data (in black) resulting from the (b) first iteration within wave equation tomography using starting velocity model shown in Figure 6a) and (c) final result after 99 iterations within wave equation tomography (the final velocity model is shown in Figure 6b). For better visibility, the traces are shown at every 50 m source-receiver offset.

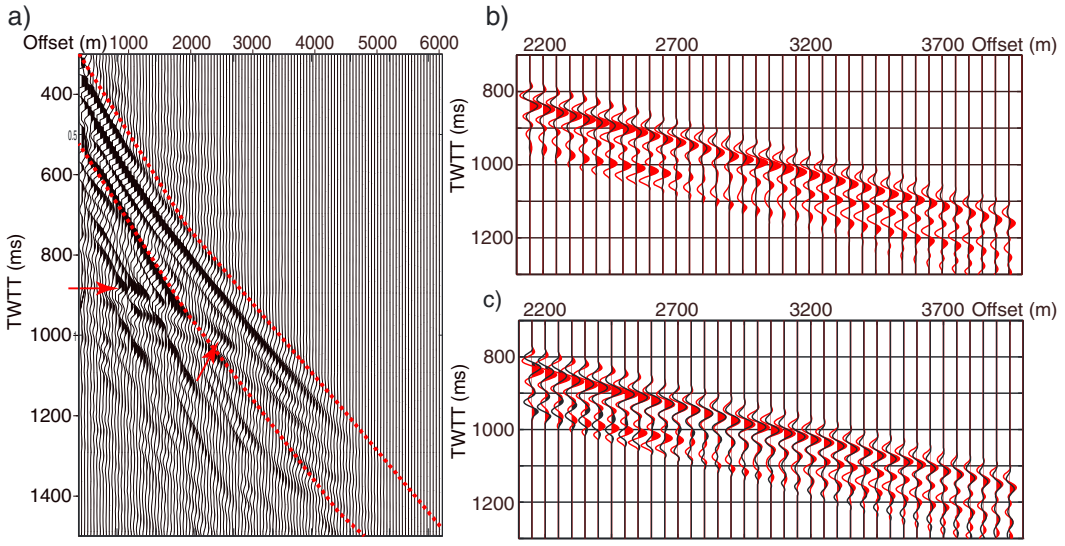

Figure 5. (a) Shot gather after the application of wave equation redatuming extracted from ~9°52′N. For better visibility, every twentieth trace is shown. The red arrows mark the presence of the AML reflector; dashed lines indicate the top and bottom mute used to define a portion of the data for which waveform inversion is done. Note that portion of the AML wide-angle reflection signal falls within thus defined mutes. Comparison of observed data (in red) and synthetically calculated data (black) resulting from (b) the first iteration using waveform inversion technique, the final velocity model obtained from wave equation tomography is used as the starting velocity for the waveform inversion (Figure 6b), and (c) the 50th iteration using waveform inversion (the final velocity model is shown in Figure 7b). Note that the satisfactory match in traveltime and phase is already obtained using wave equation tomography. For visibility, the traces are shown at every 50 m of source-receiver offset.

3.3.4. Source Wavelet

A careful estimate of a source wavelet is important in the inversion process. Although far field source signature for the MGL0812 experiment was not available, we were able to model notional source wavelets for each of the individual air guns and obtain an estimate of the far-field source wavelet. The notional wavelets for each gun are calculated using source modeling package Nucleus® (available at Lamont Doherty Earth Observatory) that requires knowledge of geometry of the gun array used in the survey, type and volume of each air gun, operating air pressure and the details of the data logger instrument filters, and sound speed of the water (Sargent et al., 2011). The modeled source signature (Figure S4a) was calculated for the source arrays geometry valid for the EPR survey, using a linear superposition of the notional signals (Figure S5). As in the inversion process, we use absorbing surface model, and we do not deghost the data (challenging for pressure data), but rather add a ghost to the far-field signal (Figure S4b). This signal is further filtered and used to produce synthetic data that are compared with the recorded data with the same dominant frequency (Figures S4c and S4d).

To evaluate the stability of the modeled source throughout the survey, we compare it with the direct waves recorded on the first trace extracted from every 100 shots (Figure S6), as the direct waves in the marine environment are independent of geology. Although the correlation coefficient is satisfactory ($>$0.85) for all of the examined shots, differences are observed in the ghost signal, especially for the shots between ~2,300 and 2,800. They are represented by irregular, small peaks, which cannot be explained by modeling. Most probably they originate from the sea condition characterized by strong swells (5–6 on Beaufort scale) due to the Elida storm that was passing to the north of the area and was affecting the nominal depth of the streamers (7.5 m). However, this noise signal has different frequency content, and the most of it was removed by data filtering.

4. Results

4.1. Redatumed Data

In the original shot gathers, the refraction branch from the upper crust is observed as a relatively weak event, which emerges at ~3,000 m source-receiver (streamer) offset (Figure 3). After data processing and wave

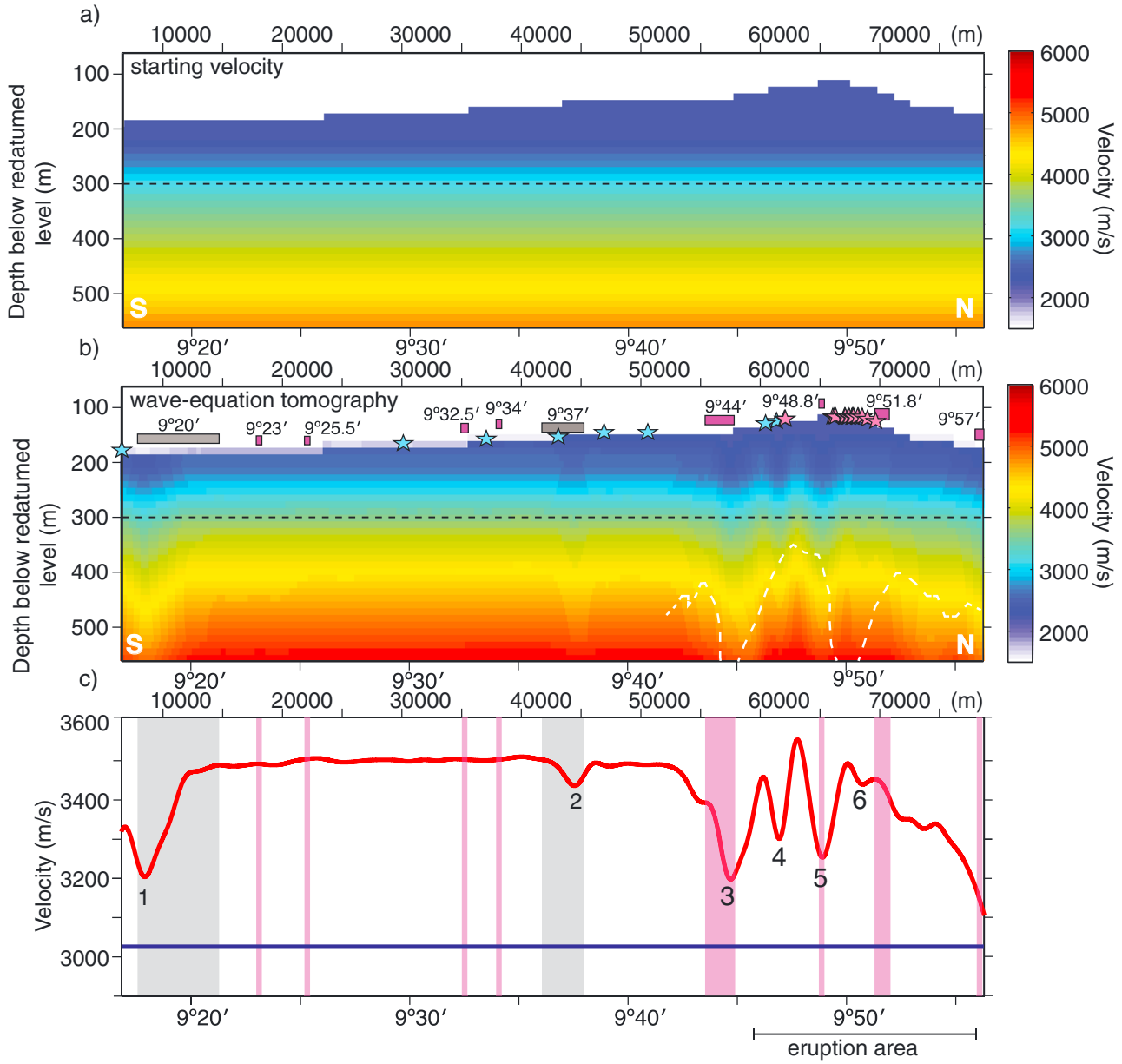

Figure 6. Velocity profiles: (a) 2-D starting velocity model obtained from 1-D ESP8 velocity function (Figure S3b; Vera et al., 1990), hung from the shallowest bathymetry level. (b) Final velocity model obtained after 99 iterations using wave equation tomography. Location of hydrothermal vents is shown in pink (Fornari et al., 2012) and blue (Haymon et al., 1991) stars (location of the individual vents is listed in Table S1), while third- and fourth-order tectonic discontinuities, with latitudes indicated, are shown in gray and purple rectangles, respectively. White dashed line is a 5,000 m/s velocity isoline extracted from the work of Newman et al. (2010). (c) Horizontal, 1-D velocity profiles extracted at 300 m below the redatumed level (~2,700 m below sea surface) from starting velocity model shown in blue and final wave equation tomography velocity model shown in red. Location of these velocity profiles is shown in dashed line in Figures 6a and 6b. The anomalies are numbered for easier identification. The fine-scale, third- and fourth-order tectonic segmentation is shown in gray and purple shaded areas, respectively. The extent of the eruption area is shown at the bottom of the profile.

equation-based redatuming, the refraction event becomes more prominent and can be tracked from 1,000 m to about 5,000 m offset (Figures 4a, 5a, and S7a). We do not show the first several hundred meters of the offset as they are affected by the applied taper. Although the refraction event in the extrapolated shots spans more than 75% of the offset, our synthetic data modeling (Figure 2) suggests that only offsets between 2,000 and 4,000 m can be used for further wave equation inversion. It is worth noting that in some of the redatumed shot gathers signal from wide-angle reflections from the AML becomes very prominent and is included in the waveform inversion.

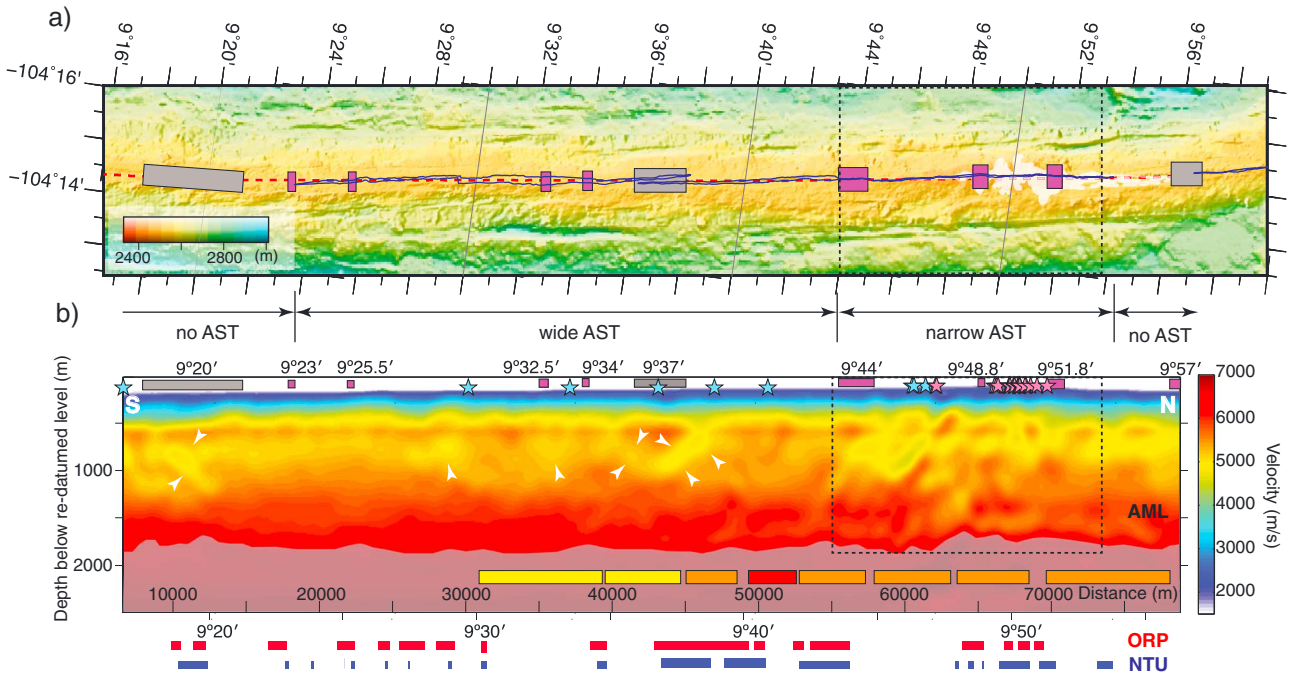

Figure 7. (a) Composite bathymetry map from multibeam sonar data acquired during the cruise and bathymetry data collected by White et al. (2006); the third- and fourth-order tectonic discontinuity zones are marked in gray and purple rectangles, respectively; the location of the 2-D seismic line is shown in dashed red line, while the dark blue one outlines the AST (Soule et al., 2009) with the description of AST character and extent given at the bottom of the panel; the white shaded area shows the extent of the lava flow emplaced during the last documented eruption. (b) Final velocity model obtained after 50 iterations of the waveform inversion. Location of hydrothermal vents active after the 2005–2006 eruption is shown in pink stars (Fornari et al., 2012). The blue stars indicate locations of the vents extracted from earlier studies (e.g., Haymon et al., 1991). The yellow, orange, and red rectangles represent interpretation of melt distribution along the EPR from Marjanović et al. (2015) where yellow represents solidified to mushy, orange mostly molten, and red highly molten portions of the AML segments defined by Carbotte et al. (2013). The red and blue rectangles at the bottom show signal from ephemeral, oxidation-reduction potential (ORP) and broadly dispersing nephelometric turbidity units (NTU), respectively, from Baker et al. (2016). While the NTU detects particle-rich, hot ($>$ 100°C), mineral-enriched discharge, the ORP detects particle-poor venting at all ranges of temperatures. The white arrowheads mark locations of the anomalies outside of the eruption zone. Shaded gray area masks less reliable part of the velocity model. The area outlined by dashed rectangle is shown in more detail in Figure 8.

4.2. Velocity Model From Wave Equation Tomography

Among the three starting velocity models that we use for wave equation tomography, the model using the 1-D smoothed ESP5 velocity function (Figure S3a) yielded the largest misfit. The misfit after the first iteration jumps to 160% of the initial misfit due to high nonlinearity. It remains above 100% even after 99 iterations, suggesting that the initial ESP5 velocity model is not suitable for linearized inversion. The presence of higher velocities in the upper crust in the ESP5 model may be the hindering factor for the wave equation tomography. In contrast, the misfit functions for the remaining two models (smoothed ESP8, and a combination of ESP8 and ESP5; Figure S3a) after 99 iterations converged to $<$10% (Figure S8a). In both cases, the resulting velocity models show very similar velocity variations (Figures S3c and S3d). To choose the preferred model for the waveform inversion, we compared the observed and calculated data for every 25th shot gather included in the inversion. We conclude that the inversion obtained using the smoothed ESP8 as the initial model obtained by extending this function in 2-D (Figure 6a) provides a better fit: the traveltime difference is reduced from average 88 ms to ~12 ms after 99 iterations of the wave equation tomography (Figure S8b). The expected maximum penetration depth is between 600 and 800 m (Figure S9).

Although the main purpose of the wave equation tomography is to provide us with the starting velocity model for further waveform inversion, the results already show some interesting features (Figure 6b). The most prominent velocity perturbations are observed north of 9°42′N over a region extending ~22 km, represented as a zone of alternating low and high velocities. The above can be readily observed in the 1-D horizontal velocity profile at 300 m depth below the redatuming level (Figure 6c). At this given depth level, four anomalies can be identified with velocity $>$ 200 m/s lower than the background velocity. The maximum width of the anomaly marked by number 3 is ~6 km, while the anomalies marked by 4 and 5 are for

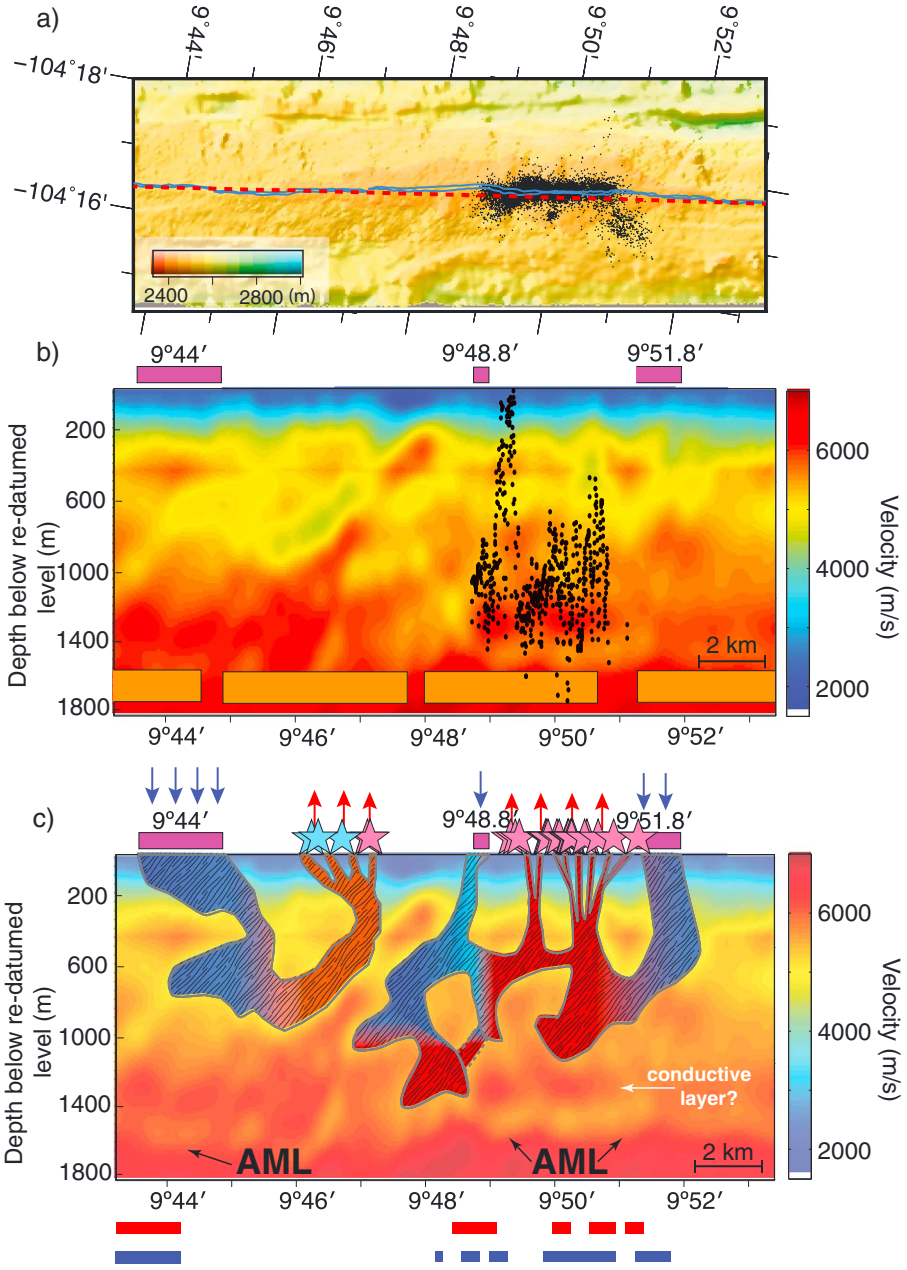

Figure 8. A close-up view (outlined in Figure 7b) on (a) bathymetry with a plan view of microearthquake locations (Waldhauser & Tolstoy, 2011) represented by black dots. The symbols are the same as in Figure 7a; (b) the 2-D velocity profile of the eruption area. The location of microearthquakes that fall within the plane of the 2-D seismic line used in this study is superimposed; (c) velocity profile with the suggested interpretation of the hydrothermal flow with red arrows indicating upflow and blue arrows indicating downflow. The remaining symbols are the same as in Figure 7b.

~2 km narrower. The anomaly marked by number 6 is the widest; it initiates at ~9°50.2′N and extends toward the end of the profile. In addition, two low-velocity zones are observed around 9°20′ (anomaly marked by number 1) and 9°37′N (number 2). The low-velocity anomaly beneath the 9°20′N is more prominent; it is ~5 km wide and is ~500 m/s lower than the surrounding velocity. The zone beneath the 9°37′N is narrower (~1 km) with a decrease in velocity ~100 m/s, at 300 m below the redatumed level (Figure 6c).

4.3. Velocity Model From Waveform Inversion

We run 50 iterations of the elastic waveform inversion. The plateau of ~45% variance reduction is reached after ~30 iterations (Figure S8a). The resulting velocity model shows more pronounced low-velocity

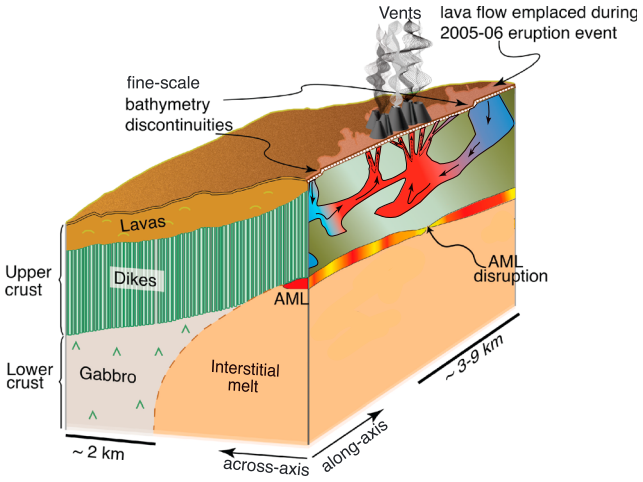

Figure 9. An illustration of processes taking place at the EPR compiling results on the hydrothermal circulation (this study), presence of the AML, its magmatic segmentation (Carbotte et al., 2013), and melt distribution (Marjanović et al., 2015). The blue and red regions with arrows superimposed indicate the presence of downgoing and upgoing pathways of a hydrothermal cell (as in Figure 8c), present within the upper crust. The remaining parts are marked in the figure.

anomalies (Figure 7b), sharpened due to the additional information contained in the amplitude and wide-angle reflection arrivals (Figures 5 and S7). For instance, the anomaly imaged at 9°20′N is similar in extent to the one imaged by the wave equation tomography but shows more details, that is, the presence of northward dipping, channel-like structure. Furthermore, the anomaly ~9°37′N becomes more significant in the waveform inversion model. It is imaged as a complex, opposed dipping structure. The northern, southward dipping feature is represented by ~500 m/s lower velocity than surrounding area. In contrast, the southern feature one is less prominent; it dips northward and is represented by velocity that is only about a couple of 100 s m/s lower than the background. The dip angle is around ~12° for both structures.

The region north of 9°42′N remains the most complex zone in the velocity model (Figures 7b and 8b). The evident vertical anomalies (Figure 6 b) present in the wave equation tomography model are reshaped and represented with more elongated and, in general, southward dipping features. This is especially visible for the anomaly centered at 9°46′N.

Extending the mute window for additional 200 ms to include signal from wide-angle reflection in waveform inversion enabled the resolving power to penetrate deeper into the crust and map low-velocity zone (Figures 7b and S10). The mapped low velocity, for ~500 m/s lower than the surrounding, we attribute to the presence of the AML. The magnitude of this anomaly might be underestimated as it is recovered from a limited portion of its wide-angle signal (e.g., Figure 5a).

All the upper crustal anomalies that we discussed are more than 1,000 m wide and are imaged down to about 1,000 m below the seafloor; their dimensions are much larger than the resolution limitation of the waveform inversion techniques we use (Figure S11).

5. Discussion

In the following subsections, we further describe and discuss the observed upper crustal low-velocity anomalies and roughly estimate the average permeability that we associate with them. Besides the velocity anomalies in the upper crust, we discuss the presence of intracrustal magma lenses (AMLs) and speculate about the possible existence of conductive layer above the AMLs (Figure 8). Furthermore, based on the geographical distribution of the low-velocity anomalies observed in the upper crust, we attribute them to hydrothermal pathways within the frame of the along axis, single-pass hydrothermal cell model (Lowell & Germanovich, 2004). The final interpretation for the eruption area is illustrated in Figure 9.

5.1. Low-Velocity Zones in the Upper Crust

In the wave equation tomography model, we image six vertical anomalies, variable in magnitude and horizontal extent (Figure 6c). While within the eruption area we clearly image four distinct anomalies (marked by numbers 3 to 6), an earlier, ray-based tomography study conducted on the same data set, with the similar redatuming approach, showed the presence of only two low-velocity anomalies comparable in amplitude and general shape but somewhat wider (Figure 6b) (Newman et al., 2010). It appears that this earlier study, due to the heavy regularization in the ray-based technique, was not able to resolve the existence of the smaller anomalies, such as the ones marked by numbers 4 and 6 (Figure 6c). Instead, they were imaged as integral parts of the nearby, bigger anomalies (3 and 5), making them ~1 km wider.

These vertical, relatively simple in shape anomalies revealed by the wave equation tomography are further modified by application of subsequent waveform inversion (compare Figures 7b and S12). In the final model, they show more complexity in geometry and variations in their width and magnitude. Some of the anomalies show channel-like forms (e.g., 9°20′, 9°37′, and 9°46′N) with the amplitudes that are for >500 m/s lower than the background velocity (Figure 7b). The most prominent anomaly is observed ~9°46′N, as southward dipping channel with the velocity drop ~1,000 m/s. The presence of this structure has been imaged in

depth-migrated seismic section (Figure S13), confirming its plausibility. A comparable dipping event in depth-migrated seismic section corresponds to the anomaly north of 9°37′N. It is interesting to note that although the dipping direction varies, for all of the pipe-like anomalies the dipping angle is approximately the same (~12°), which could potentially indicate a similar mechanism behind its origin. A propagation of the tectono-magmatic segments could be one of the components of this mechanism. It is known that the northern (north of the OSC 9°03′N), second-order segment has exhibited a long-term predominantly southward ridge propagation (Carbotte & Macdonald, 1992). On this global ridge migration, a local propagation of the higher-order ridge segments may have been superimposed. Such complex propagation mechanism has been observed elsewhere along the fast-propagating ridge system, for example, the Southern EPR (Cormier & Macdonald, 1994). The examination of the high-resolution bathymetry along the EPR (White et al., 2006) shows the presence of small propagating wakes, imaged as discordant features of disturbed seafloor fabric behind the segment's tip. The orientation of the imaged features indicates that the higher-order segments north of 9°46′ and 9°37′N have been predominantly propagating southward, while the segment south of 9°20′N has been propagating northward (Figure S14). The agreement in the sense of propagation and dip orientation of the velocity anomalies suggests that processes taking place in the upper crust and perhaps all the way to the AML level could have an important role in the propagation of the higher-order segments. If correct, it would also imply that these velocity lows are not ephemeral features. However, for further discussion, implications, and rate of propagation, more detailed examination of bathymetry and comparison with other geophysical data sets (e.g., gravity and magnetics) need to take place.

In contrast to well-developed, channel-shaped anomalies, the region north of 9°48′N is characterized by geometrically more complex anomalies (Figures 7b and 8b). The irregular forms we observe are most probably caused by repetitive eruption/diking events within the region (Germanovich et al., 2011; Haymon et al., 1993; Sohn et al., 1998; Waldhauser & Tolstoy, 2011) that have been reshaping the permeability of the upper crust within the eruption area.

5.2. Permeability of the Zero-Age Crust

The permeability of the rocks is believed to be the primary controlling factor for the fluid circulation within MOR hydrothermal systems (Fisher, 1998, 2004). Thus, a significant effort has been put to define permeability from seismic attributes and obtain further insights on the intensity of hydrothermal convection and geometry of the flow. A number of empirical porosity/permeability and velocity relationships have been derived (e.g., Berge et al., 1992; Carlson, 2010; Carlson & Herrick, 1990; Carlson & Raskin, 1984; Wilkens et al., 1991) with the most recent compilation focused in particular on the relationship(s) valid for the upper crust formed at fast to intermediate MOR (Carlson, 2014). Using the relationship from this latest study and average velocity from our low-velocity anomalies (~4.5 km/s) for porosity, we obtain wide range of values varying from 2.5 to 14%, depending on the fractional area of asperity contact (Af) ranging from 0.003 to 0.09 (depicted in Figure 6 in Carlson, 2014). From thus estimated porosity, permeability is derived from modified Kozen-Carmen model (Carlson, 2011). By assuming Af~0.05 (Carlson, 2014) and average porosity of ~8%, for permeability within our low-velocity anomalies we obtain ~$10^{-13.2}$ m^2, which falls within the range of permeability values commonly used in modeling of hydrothermal flow (e.g., Fehn et al., 1983; Fontaine et al., 2011; Hasenclever et al., 2014; Ribando et al., 1976). Following the same approach, we estimate the permeability of the rock outside of the inferred hydrothermal pathways and obtain value around 10^{-16} m^2. Our results suggest important permeability variation of the zero-age crust, which is commonly overlooked in the hydrothermal models for the MOR system (e.g., Hasenclever et al., 2014). A similar order of variation in permeability of the young crust at 9°50′N was inferred by modeling of crustal stresses using poroelastically triggered earthquakes, with values ranging from $10^{-9.4}$ to $10^{-13.4}$ m^2 (Crone et al., 2011). The discrepancy between the latter and our estimates most probably originates from assumptions in both approaches. In our case, permeability estimates are highly affected by uncertainties related to our modeling parameters and their effects on the absolute values of velocities (2-D modeling of 3-D space, underestimated magnitude of low-velocity anomalies, assuming isotropic subsurface, just to name a few), along with the uncertainties in empirically derived velocity and porosity/permeability relationships (Carlson, 2014).

5.3. Intracrustal Melt

In addition to the upper crustal variations in velocities, we also image a subhorizontal, low-velocity zone at ~1,500 m below the seafloor, visible north of 9°43′N that we attribute to the presence of the AML, a heat

source for the onset and maintenance of hydrothermal activity (Figures 7b, 8, and S10). The strongest low-velocity signal is observed around 9°50′N (about 500 m/s lower than the surrounding), where the AML is defined as mostly molten, with prominent patches of highly molten regions (Marjanović et al., 2015). It is also the area of hydrothermal discharge (Baker et al., 2016; Fornari et al., 2012), supporting the idea that permeability and thermal regime are equally important in determining the distribution of vent sites (Canales et al., 2006; Singh et al., 1999).

Elsewhere, the signal of low-velocity anomaly is weak (<200 m/s) and in places, it is contrasting with the results from previous studies on melt distribution (Marjanović et al., 2015; Xu et al., 2014). For instance, while the AML segment extending between 9°40 and 42′N was characterized as a highly molten region, with bright reflection and shear velocities dropping to zero (Xu et al., 2014), the 2-D waveform inversion shows only slight change in velocity (<100 m/s). This observed discrepancy we attribute to the fact that the 2-D inversion was mainly targeting the refraction event within the midoffsets (for imaging the upper crust), within a limited time window that was kept constant along the seismic line; thus, any change of the AML reflection signal with offset and/or its depth was not captured with our 2-D modeling. The above view is supported by comparison of shots gathers extracted from the two contrasting regions (Figures 5 and S7). In Figure 5 the shot gather is extracted at the location in the vicinity of 9°52′N where the AML appears as a strong event that can be tracked up to 3,000 m offset, the portion of which is included by the defined inversion window and translated to low-velocity anomaly in the waveform inversion model. In contrast, although the shot gather extracted ~9°40′N (Figure S7) shows bright AML reflector, none or a very small portion of the AML reflection signal is encompassed by the inversion window (the event appears at greater twtt) and thus no information on the AML was included in our waveform inversion modeling. For further, proper evaluation of the AML signal the application of emerging techniques, such as reflection-based full-waveform inversion (e.g., Gomes & Chazalnoel, 2017) or localized full-waveform inversion (e.g., Yuan et al., 2017), is recommended. The region south of 9°37′N does not show the presence of the velocity anomaly that could be related to the AML. This is not surprising, as the reflection signal from the AML in this region is weak (almost absent in the shot gathers).

Nevertheless, the comparison between results from Marjanović et al. (2015) (using the same data set as presented here) and recent hydrothermal activity signal shows relatively good spatial correlation between magmatically robust portions of the ridge and incidence of venting. The exception is the region extending between 9°44′ and 9°48′N for which mostly molten AML is present but no venting is reported in the recent plume study (Baker et al., 2016).

5.4. Conductive Layer

A relatively thin (<250 m) conductive layer or hydrothermal root zone is a thermal boundary layer between two convective systems, the AML below and sheeted dikes complex above (Chenevez & Nicolas, 1997; Gillis & Roberts, 1999; Nicolas & Boudier, 1991). This layer is characterized by a large temperature gradient of about 800°C: from ~1,200°C at the top AML to l,400–450°C at the base of the hydrothermally cooled dikes. Its presence has been proposed by a number of numerical hydrothermal models (e.g., Germanovich et al., 2000; Lowell & Burnell, 1991) and observations from ophiolites (e.g., Gillis, 2002; Gillis & Roberts, 1999; MacLeod & Yaouancq, 2000; Nicolas & Boudier, 2011; Pedersen, 1986). Its existence was confirmed within the cores extracted from the IODP Hole 1256D in the eastern Pacific Ocean (Nicolas et al., 2008; Wilson et al., 2006) and at the southern EPR in seismic data using 1-D full waveform-inversion technique (Singh et al., 1999). In 1-D velocity profile it is seen as a rather thin <80 m higher-velocity zone (for ~1 km/s higher than the dike section above) on top of the AML. In our final model, north of 9°44′N low-velocity zone, we interpret as the presence of the AML (Figures 8b and S10), is overlain by 100–150 m thick high velocity layer (~800 m/s higher than the dike section), which could be interpreted as conductive layer, marking the depth of hydrothermal fluid penetration.

5.5. Hydrothermal Pathways Within the Upper Crust

The upper crustal low-velocity/high permeability anomalies from our model we attribute to potential hydrothermal pathways (Figures 8c and 9). Based on the shape and magnitude of the anomalies we can only speculate about the sense of fluid circulation within them. However, spatial correlation with other geological features, such as the higher-order tectonic discontinuities (Carbotte et al., 2015; White et al., 2006) and

presence of hydrothermal venting sites (Baker et al., 2016; Fornari et al., 2012), can be used to propose a plausible model of detailed hydrothermal circulation with its upgoing and downgoing flow.

Some of the most prominent low-velocity anomalies seem to be spatially correlated with the two third-order tectonic discontinuities centered at ~9°20′ and 9°37′N (Figures 6b, 6c, and 7b). In bathymetry, these two locations appear as the OSCs, with ~3 km long overlapping zone, offset by 0.5–1 km (White et al., 2006). These morphotectonic features have been undergoing constant tectonic deformation for at least several hundreds kyr, which corresponds to the longevity of a third-order discontinuity (e.g., Carbotte et al., 2013). As a result these sites are likely to be fractured and well suited for hydrothermal circulation due to enhanced fracturing. However, in the vicinity of these discontinuities, except for the few single vent sites, the earlier studies did not identify the presence of an active hydrothermal venting site (Figure 7b and Table S1) (e.g., Beaulieu et al., 2013; Haymon et al., 1991).

Results from the recent plume study (Baker et al., 2016) denote, in contrast, the presence of hydrothermal discharge spatially correlated with the velocity anomalies we image beneath these two third-order discontinuities (Figure 7b). For the 9°20′N the extent of the velocity anomaly within the upper crust matched well with the extent of relatively low hydrothermal signal captured ~60 m above the seafloor, indicating the presence of at least diffusive venting site(s). In contrast, the complex anomaly depicted in our model ~9°37′N is matched by a stronger hydrothermal signal. The shallow portion of the imaged conflicting dip velocity anomaly (Figure 7b) coincides with the prominent peaks in both broadly dispersing, light backscattering and ephemeral tracers (Baker et al., 2016). This strong spatial correlation suggests that within this area the imaged low-velocity anomalies are most probably associated with the hydrothermal upflow. However, it needs to be mentioned that the hydrothermal discharge signal similar in character is captured farther to the north (up to 9°41′N), but no evident perturbation in velocity is observed. This could be due to the fact that both studies are snapshots of the hydrothermal processes, and that the 3 years of the time lag between the two studies may have played an important role in the observed differences. Also, our seismic study is an image of the subsurface within the 2-D axis-centered plane that does not capture variations in rock properties laterally. The latter reasoning can also be evoked to explain why no velocity anomaly is observed directly beneath the 9°37′N OSC that is considered as an ideal place for a downflow to develop.

The region extending between the 9°20′N and 9°37′N third-order discontinuities is characterized by four fourth-order tectonic discontinuities (Figure S14) (Carbotte et al., 2013, 2015) but no prominent velocity anomalies (Figure 7b). Here the earlier data mapped only a couple of vent edifices, indicating limited hydrothermal activity (e.g., Haymon et al., 1991). The recent, more systematic study by Baker et al. (2016) showed the presence of plume signal within this region. However, the signal is discontinuous and mainly present in the oxidation-reduction potential (ORP) tracers (Figure 7b), which suggests that the hydrothermal activity is represented mostly by diffuse venting with the possible presence of discrete chimneys where the nephelometric turbidity unit (NTU) anomaly appears, for example, the localized region ~9°25.5′ and 9°29′N. Both of these regions are underlaid by moderate velocity anomalies ($<$200 m/s smaller than the surroundings). It is important to note that the AML signal within this region is also weak, suggesting low thermal regime (Carbotte et al., 2013), insufficient for developing focused high-temperature venting.

The most complexities in the velocity model(s) we observe north of ~9°44′N that roughly corresponds to the area of the last documented eruption (e.g., Tolstoy et al., 2006). Here all three fourth-order tectonic discontinuities (Figure S14) are underlined by a velocity low (Figures 7b and 8). For instance, the discontinuity identified as the change in the width of the AST at 9°44′N (Figures 7a, 8a, and S14) is underlaid by a geometrically complex, 3 km wide low-velocity anomaly sitting at ~750 m below the redatumed level (or ~650 m below the seafloor). The above suggests it as a zone of the hydrothermal recharge. Interestingly, the southern edge of the discontinuity zone and the region ~1.5 km south of it were indicated as regions with the presence of hydrothermal discharge (Baker et al., 2016). However, the most of this plume anomaly is not matched by our velocity model. One of the possible explanation is that the hydrothermal activity has developed after our seismic survey.

The remaining two discontinuities at 9°48.8′N (change in the AST width) and 9°51.8′N (deviations in ridge axis lineation; Figure S14) are underlaid by smaller in extent, but similar in amplitude, low-velocity anomalies (Figure 8b). We interpret them as the locations where hydrothermal recharge is taking place. The view that this fourth-order tectonic discontinuity could represent the on-axis locations where seawater can

penetrate the crust was also evoked to interpret the 2003–2004 microearthquakes swarm pattern (Tolstoy et al., 2008). The origin of the prominent pipe-like cluster of earthquakes at 9°49.25′N was interpreted as a thermal contraction of the rock when in contact with cold seawater, taking place within the zone of the nearest fourth-order discontinuity (Waldhauser & Tolstoy, 2011) (Figure 8b). However, detailed mapping of the seafloor showed that the exact location of the discontinuity is limited to couple of hundreds of meters around 9°48.8′N (Carbotte et al., 2013). The latter shows that the cluster is located >1 km to the north of the discontinuity and the low-velocity anomaly, we interpret as the presence of downgoing flow. The northward shift of the cluster and mismatch with our interpreted downgoing flow could be attributed to the inadequacy of the 1-D velocity function used for locating the microearthquakes (Waldhauser & Tolstoy, 2011). Thus, any further comparison between our velocity model and microearthquake pattern is not possible.

North of the 9°48.8′ discontinuity we observe two velocity lows that are sitting right beneath the vents that remained active after the 2005–2006 eruption event (Fornari et al., 2012; Von Damm, 2006) and were showing important hydrothermal venting activity in the more recent study (Baker et al., 2016). In particular, the anomaly centered at 9°50.6′N is matched perfectly with the extremes both in NTU and ORP traces. We attribute these anomalies to the active upflow pathways.

Finally, the most prominent low-velocity anomaly within the eruption area is centered at 9°46.5′N, located beneath the southern cluster of vent sites, some of them still active after the 2005–2006 eruption (Fornari et al., 2012). However, the recent plume data indicate this region devoid of any hydrothermal signal (Baker et al., 2016). Several explanations mutually inclusive can be offered to explain the observations. It could be that right after the eruption the pathways were still opened, and thus the vents were confirmed active (Fornari et al., 2012). However, at some point in time, the pathways became clogged either by mineral precipitation (Fontaine et al., 2001; Lowell et al., 2013) or/and tectonic reorganization of the pathways associated with the eruption. This perturbation in the upper crustal structure may have occurred after our survey that took place in 2008, and thus we image the upgoing flow that was active at that time. However, it is also possible that the timescale of changes in the structure of the upper crust and thus modeled velocities are much longer than the timescale of changes in hydrothermal processes (Baker, 2009).

6. Conclusions

We present high-resolution 2-D models within which we image prominent low-velocity anomalies that we attribute to the presence of hydrothermal circulation system signatures within the along-axis plane of the EPR. The low-velocity anomalies directly beneath venting sites mapped in the seafloor we attribute to the pathways along which hot, particle-enriched hydrothermal fluids are migrating upward, toward the seafloor. In contrast, the low-velocity zones imaged within or in the vicinity of known higher-order, morphotectonic deformations we interpret as ideal locations for the cold water to penetrate the crust and potentially establish downgoing pathway. Whether a hydrothermal flow will be established through those predefined tectonically weakened zones on the ridge axis does not depend only on the presence of high crustal permeability but also on their spatial correlation with the heat source (i.e., AML) and its magmatic robustness (presence of AML molten portions). Our results strongly suggest that well developed, focused hydrothermal venting is a result of close synergy between the enhanced tectono-magmatic processes on small spatial scales. Such conditions are met within the eruption area where three hydrothermal cells are fully developed (two of which have a common upflow) and display important geometrical complexities.

Acknowledgments

We would like to thank Suzanne M. Carbotte, John C. Mutter the PIs, and Mladen R. Nedimović and Juan Pablo Canales the CoPIs of the MGL0812 experiment during which the data were collected. We are also very grateful to Omid Aghaei and Gabriel Huot for their help with data processing, and Hanchao Jian and Hayang Wang for their useful advice on the wave equation tomography inversion code. We also acknowledge the contribution of Lindsey Doermann and Hélène Carton on source signal modeling. In addition, we would like to acknowledge the comments and suggestions of Edward Baker, Richard Davy, and of the Associate Editor that significantly improved the manuscript. This work is funded by Marie S. Curie grant awarded to Milena Marjanović within the call: H2020-H2020-MSCA-IF-2014, 655283. Numerical computations were performed on the S-CAPAD platform, IPGP, France. All MCS field data collected along the ridge axis are archived at Academic Seismic Portal (doi:10.7284/901987).

References

Aghaei, O. (2013). The East Pacific Rise crustal thickness, Moho transition zone character and off/axis magma lens melt content from 9°37.5′N to 9°57′N: Results from three-dimensional multichannel seismic data analysis, PhD Thesis, Dalhousie University, Halifax, Canada.

Aghaei, O., Nedimović, M. R., Carton, H., Carbotte, S. M., Canales, J. P., & Mutter, J. C. (2014). Crustal thickness and Moho character of the fast-spreading East Pacific Rise from 9°42′N to 9°57′N from post-stack migrated 3-D MCS data. *Geochemistry, Geophysics, Geosystems*, *15*, 634–657. https://doi.org/10.1002/2013GC005069

Arnulf, A. F., Singh, S. C., Harding, A. J., Kent, G. M., & Crawford, W. (2011). Strong seismic heterogeneity in layer 2A near hydrothermal vents at the mid-Atlantic ridge. *Geophysical Research Letters*, *38*, L13320. https://doi.org/10.1029/2011GL047753

Arnulf, A. F., Harding, A. J., Singh, S. C., Kent, G. M., & Crawford, W. (2012). Fine-scale velocity structure of upper oceanic crust from full waveform inversion of downward continued seismic reflection data at the Lucky Strike volcano, mid-Atlantic ridge. *Geophysical Research Letters*, *39*, L08303. https://doi.org/10.1029/2012GL051064

Arnulf, A. F., Harding, A. J., Singh, S. C., Kent, G. M., & Crawford, W. (2014). Nature of upper crust beneath the Lucky Strike volcano using elastic full waveform inversion of streamer data. *Geophysical Journal International*, *196*(3), 1471–1491. https://doi.org/10.1093/gji/ggt461

Arnulf, A. F., Harding, A. J., Kent, G. M., Carbotte, S. M., Canales, J. P., & Nedimović, M. R. (2014). Anatomy of an active submarine volcano. *Geology*, *42*(8), 655–658. https://doi.org/10.1130/G35629.1

Baker, E. T. (2009). Relationships between hydrothermal activity and axial magma chamber distribution, depth, and melt content. *Geochemistry, Geophysics, Geosystems*, *10*, Q06009. https://doi.org/10.1029/2009GC002424

Baker, E. T., & German, C. R. (2004). On the global distribution of hydrothermal vent fields. In C. R. German, J. Lin, & L. M. Parson (Eds.), *Mid-ocean ridges: Hydrother-mal interactions between the lithosphere and oceans*, *Geophysical Monograph Series* (Vol. 148, pp. 245–266). Washington, DC: American Geophysical Union.

Baker, E. T., Feely, R. A., Mottl, M. J., Sansone, F. T., Wheat, C. G., Resing, J. A., & Lupton, J. E. (1994). Hydrothermal plumes along the East Pacific Rise, 8°40′ to 11°50′N: Plume distribution and relationship to the apparent magmatic budget. *Earth and Planetary Science Letters*, *128*(1-2), 1–17. https://doi.org/10.1016/0012-821X(94)90022-1

Baker, E. T., German, R. G., & Elderfield, H. (1995). Hydrothermal plumes over spreading-center axes: Global distributions and geological inferences. In *Seafloor hydrothermal systems: Physical, chemical, biological, and geological interactions*, *Geophysical Monograph 91* (pp. 47–70). Washington, DC: American Geophysical Union.

Baker, E. T., Resing, J. A., Haymon, R. M., Tunnicliffe, V., Lavelle, J. W., Martinez, F., … Nakamura, K. (2016). How many vent fields? New estimates of vent field populations on ocean ridges from precise mapping of hydrothermal discharge locations. *Earth and Planetary Science Letters*, *449*, 186–196. https://doi.org/10.1016/j.epsl.2016.05.031

Beaulieu, S. E., Baker, E. T., German, C. R., & Maffei, A. (2013). An authoritative global database for active submarine hydrothermal vent fields. *Geochemistry, Geophysics, Geosystems*, *14*, 4892–4905. https://doi.org/10.1002/2013GC004998

Beaulieu, S. E., Baker, E. T., & German, C. R. (2015). Where are the undiscovered vents on oceanic spreading ridges? *Deep Sea Research*, *121*, 202–212. https://doi.org/10.1016/j.dsr2.2015.05.001

Bemis, K., Lowell, R. P., & Farough, A. (2012). Diffuse flow on and around hydrothermal vents at mid-Ocean ridges. *Oceanography*, *25*, 182–191. https://doi.org/10.5670/oceanog.2012.16

Berge, P. A., Fryer, G. J., & Wilkens, R. H. (1992). Velocity-porosity relationships in the upper oceanic crust: Theoretical considerations. *Journal of Geophysical Research*, *97*(B11), 15,239–15,254. https://doi.org/10.1029/92JB01464

Berryhill, J. R. (1979). Wave-equation datuming. *Geophysics*, *44*(8), 1329–1344. https://doi.org/10.1190/1.1441010

Berryhill, J. R. (1984). Wave-equation datuming before stack. *Geophysics*, *49*(11), 2064–2066. https://doi.org/10.1190/1.1441620

Blacic, T. M., Ito, G., Canales, J. P., Detrick, R. S., & Sinton, J. (2004). Constructing the crust along the Galapagos spreading center 91.3–95.5 W: Correlation of seismic layer 2A with axial magma lens and topographic characteristics. *Journal of Geophysical Research*, *109*, B10310. https://doi.org/10.1029/2004JB003066

Bonatti, E. (1975). Metallogenesis at oceanic spreading centers. *Annual Review of Earth and Planetary Sciences*, *3*(1), 401–431. https://doi.org/10.1146/annurev.ea.03.050175.002153

Brenders, A. J., & Pratt, R. G. (2007). Full waveform tomography for lithospheric imaging: Results from a blind test in a realistic crustal model. *Geophysical Journal International*, *168*, 133–151. https://doi.org/10.1111/j.1365-246X.2006.03156.x

Canales, J. P., Singh, S. C., Detrick, R. S., Carbotte, S. M., Harding, A. J., Kent, G. M., … Nedimović, M. R. (2006). Seismic evidence for variations in axial magma chamber properties along the southern Juan de Fuca ridge. *Earth and Planetary Science Letters*, *246*(3-4), 353–366. https://doi.org/10.1016/j.epsl.2006.04.032

Cannat, M., Cann, J., & Maclennan, J. (2004). Some hard rock constraints on the supply of heat to mid-Ocean ridges. In C. R. German, J. Lin, & L. M. Parson (Eds.), *Mid-Ocean ridges* (Vol. 148, pp. 111–149). Washington, DC: American Geophysical Union. https://doi.org/10.1029/148GM05

Carbotte, S., & Macdonald, K. (1992). East Pacific Rise 8°–10°30′N: Evolution of ridge segments and discontinuities from SeaMARC II and three dimensional magnetic studies. *Journal of Geophysical Research*, *97*(B5), 6959–6982. https://doi.org/10.1029/91JB03065

Carbotte, S. M., Ponce-Correa, G., & Solomon, A. (2000). Evaluation of morphological indicators of magma supply and segmentation from a seismic reflection study of the EPR 15°30′-17°N. *Journal of Geophysical Research*, *105*(B2), 2737–2759. https://doi.org/10.1029/1999JB900245

Carbotte, S. M., Detrick, R. S., Harding, A., Canales, J. P., Babcock, J., Kent, G., … Diebold, J. (2006). Rift topography linked to magmatism at the intermediate spreading Juan de Fuca ridge. *Geology*, *34*, 209–212, doi:10.113/G21969. https://doi.org/10.1130/G21969.1

Carbotte, S. M., Marjanović, M., Carton, H. D., Mutter, J. C., Canales, J. P., Nedimović, M. R., … Perfit, M. R. (2013). Fine-scale segmentation of the crustal magma reservoir beneath the East Pacific Rise. *Nature Geoscience*, *6*(10), 866–870. https://doi.org/10.1038/ngeo1933

Carbotte, S. M., Smith, D. K., Cannat, M., & Klein, E. M. (2015). Tectonic and magmatic segmentation of the global ocean ridge system: A synthesis of observations. In T. J. Wright et al. (Eds.), *Magmatic rifting and active volcanism*. *Geological Society, London, Special Publications* (Vol. 420, pp. 249–295). https://doi.org/10.1144/SP420.5

Carlson, R. L. (2010). How crack porosity and shape control seismic velocities in the upper oceanic crust: Modeling downhole logs from Holes 504B and 1256D. *Geochemistry, Geophysics, Geosystems*, *12*, Q09013. https://doi.org/10.1029/2011GC003624

Carlson, R. L. (2011). The effect of hydrothermal alteration on the seismic structure of the upper oceanic crust: Evidence from Holes 504B and 1256D. *Geochemistry, Geophysics, Geosystems*, *11*, Q04007. https://doi.org/10.1029/2009GC002955

Carlson, R. L. (2014). The influence of porosity and crack morphology on seismic velocity and permeability in the upper oceanic crust. *Geochemistry, Geophysics, Geosystems*, *15*(1), 10–27. https://doi.org/10.1002/2013GC004965

Carlson, R. L., & Herrick, C. N. (1990). Densities and porosities in the oceanic crust and their variations with depth and age. *Journal of Geophysical Research*, *95*(B6), 9153–9170. https://doi.org/10.1029/JB095iB06p09153

Carlson, R. L., & Raskin, G. S. (1984). Density of the ocean crust. *Nature*, *311*(5986), 555–558. https://doi.org/10.1038/311555a0

Castagna, J. P., Batzle, M. L., & Eastwood, R. L. (1985). Relationships between compressional-wave and shear-wave velocities in clastic silicate rocks. *Geophysics*, *50*(4), 571–581. https://doi.org/10.1190/1.1441933

Chadwick, J., Perfit, M., Ridley, I., Jonasson, I., Kamenov, G., Chadwick, W., … Smith, M. (2005). Magmatic effects of the Cobb hot spot on the Juan de Fuca ridge. *Journal of Geophysical Research*, *110*, B03101. https://doi.org/10.1029/2003JB002767

Chenevez, J., & Nicolas, A. (1997). Crustal feeding in the Oman ophiolite from the top or from the bottom? A thermal and mass balance model. *Geophysical Research Letters*, *24*(14), 1811–1814. https://doi.org/10.1029/97GL01681

Choo, J., Downton, J., & Dewar, J. (2004). LIFT: A new and practical approach to noise and multiple attenuation. *The First Break*, *22*, 39–44.

Collier, J. S., & Singh, S. C. (1997). Detailed structure of the top of the melt body beneath the East Pacific rise at 9°40N from waveform inversion of seismic reflection data. *Journal of Geophysical Research*, *102*(B9), 20,287–20,304. https://doi.org/10.1029/97JB01514

Corliss, J. B., Dymond, J., Gordon, L. I., Edmond, J. M., von Herzen, R. P., Ballard, R., … van Andel, T. H. (1979). Submarine thermal springs on the Galapagos rift. *Science*, *203*(4385), 1073–1083. https://doi.org/10.1126/science.203.4385.1073

Cormier, M. H., & Macdonald, K. C. (1994). East Pacific rise 18°–19°S: Asymmetric spreading and ridge reorientation by ultrafast migration of axial discontinuities. *Journal of Geophysical Research*, *99*(B1), 543–564. https://doi.org/10.1029/93JB02382

Coumou, D., Geiger, S., Driesner, T., Heinrich, C. A., & Matthai, S. K. (2006). The dynamics of mid-ocean ridge hydrothermal systems: Splitting plumes and fluctuating vent temperatures. *Earth and Planetary Science Letters*, *245*, 218–231. https://doi.org/10.1016/j.epsl.2006.02.044

Coumou, D., Driesner, T., & Heinrich, C. A. (2008). The structure and dynamics of mid-ocean ridge hydrothermal systems. *Science*, *321*, 1825–1828. https://doi.org/10.1126/science.1159582

Coumou, D., Driesner, T., Weis, P., & Heinrich, C. A. (2009). Phase separation, brine formation, and salinity variation at black smoker hydrothermal systems. *Journal of Geophysical Research*, *114*, B03212. https://doi.org/10.1126/10.1029/2008JB005764

Coumou, D., Driesner, T., Geiger, S., Paluszny, A., & Heinrich, C. A. (2009). High-resolution 3D simulations of mid-ocean ridge hydrothermal systems. *Journal of Geophysical Research*, *114*, B07104. https://doi.org/10.1029/2008JB006121

Crone, T. J., Tolstoy, M., & Stroup, D. F. (2011). Permeability structure of young ocean crust from poroelastically triggered earthquakes. *Geophysical Research Letters*, *38*, L05305. https://doi.org/10.1029/2011GL046820

Delaney, J. R., Robigou, V., McDuff, R., & Tivey, M. (1992). Geology of vigorous hydrothermal system on the Endeavour Segment, Juan de Fuca ridge. *Journal of Geophysical Research*, *97*(B13), 19,663–19,682. https://doi.org/10.1029/92JB00174

Detrick, R. S., Buhl, P., Vera, E., Mutter, J., Orcutt, J., Madsen, J., & Brocher, T. (1987). Multi-channel seismic imaging of a crustal magma chamber along the East Pacific rise. *Nature*, *326*(6108), 35–41. https://doi.org/10.1038/326035a0

Detrick, R. S., Harding, A., Kent, G., Orcutt, J., Mutter, J., & Buhl, P. (1993). Seismic structure of the southern East Pacific Rise. *Science*, *259*(5094), 499–503. https://doi.org/10.1126/science.259.5094.499

Detrick, R. S., Sinton, J. M., Ito, G., Canales, J. P., Behn, M., Blacic, T., … Mahoney, J. (2002). Correlated geophysical, geochemical and volcanological manifestations of plume-ridge interaction along the Galapagos spreading center. *Geochemistry, Geophysics, Geosystems*, *3*(10),8501 . https://doi.org/10.1029/2002GC000350

Dunn, R. A., Toomey, D. R., & Solomon, S. C. (2000). Three-dimensional seismic structure and physical properties of the crust and shallow mantle beneath the East Pacific rise at 9°30′N. *Journal of Geophysical Research*, *105*(B10), 23,537–23,555. https://doi.org/10.1029/2000JB900210

Fehn, U., Green, K. E., Von Herzen, R. P., & Cathles, L. W. (1983). Numerical models for the hydrothermal field at the Galapagos spreading center. *Journal of Geophysical Research*, *88*(B2), 1033–1048. https://doi.org/10.1029/JB088iB02p01033

Fisher, A. T. (1998). Permeability within basaltic oceanic crust. *Reviews of Geophysics*, *36*(2), 143–182. https://doi.org/10.1029/97RG02916

Fisher, A. T. (2004). Rates of flow and patterns of fluid circulation. In E. E. Davis, & H. Elderfield (Eds.), *Hydrogeology of the oceanic lithosphere*, (pp. 339–377). Cambridge, U. K.: Cambridge Univ. Press.

Fliedner, M. M., White, R. S., & Smallwood, J. R. (1998). Seismic velocity structure of basalt flows. *SEG Expanded Abstracts*, *SP4.5*, 1178–1181.

Fontaine, F., Rabinowicz, M., & Boulègue, J. (2001). Permeability changes due to mineral diagenesis in fractured crust: Implications for hydrothermal circulation at mid-ocean ridges. *Earth and Planetary Science Letters*, *184*(2), 407–425. https://doi.org/10.1016/S0012-821X(00)00332-0

Fontaine, F. J., Olive, J.-A., Cannat, M., Escartín, J., & Perol, T. (2011). Hydrothermally-induced melt lens cooling and segmentation along the axis of fast- and intermediate-spreading centers. *Geophysical Research Letters*, *38*, L14307. https://doi.org/10.1029/2011GL047798

Fontaine, F. J., Cannat, M., Escartin, J., & Crawford, W. C. (2014). Along-axis hydrothermal flow at the axis of slow spreading mid-Ocean ridges: Insights from numerical models of the Lucky Strike vent field (MAR). *Geochemistry, Geophysics, Geosystems*, *15*(7), 2918–2931. https://doi.org/10.1002/2014GC005372

Fornari, D. J., Tivey, M. A., Schouten, H., Perfit, M., Yoerger, D., Bradley, A., … Von Damm, K. (2004). Submarine lava flow emplacement at the East Pacific Rise 9°50′N: Implications for uppermost ocean crust stratigraphy and hydrothermal fluid circulation. In C. R. German, J. Lin, & L. M. Parson (Eds.), *Mid-Ocean ridges: Hydrothermal interactions between the lithosphere and oceans*, *Geophysical Monograph Series*, (Vol. 148, pp. 187–218). Washington, DC: American Geophysical Union.

Fornari, D. J., Beaulieu, S. E., Holden, J. F., Mullineaux, L. S., & Tolstoy, M. (2012). Introduction to the special issue: From RIDGE to ridge 2000. *Oceanography*, *25*(1), 12–17. https://doi.org/10.5670/oceanog.2012.01

Fundis, A. T., Soule, S. A., Fornari, D. J., & Perfit, M. R. (2010). Paving the seafloor: Volcanic emplacement processes during the 2005–2006 eruptions at the fast spreading East Pacific Rise, 9°50N. *Geochemistry, Geophysics, Geosystems*, *11*, Q08024. https://doi.org/10.1029/2010GC003058

Gardner, H. F., Gardner, L. W., & Gregory, A. R. (1974). Formation velocity and density—The diagnostic basics for stratigraphic traps. *Geophysics*, *39*(6), 770–780. https://doi.org/10.1190/1.1440465

Germanovich, L. N., Lowell, R. P., & Astakhov, D. K. (2000). Stress-dependent permeability and the formation of seafloor event plumes. *Journal of Geophysical Research*, *105*(B4), 8341–8354. https://doi.org/10.1029/1999JB900431

Germanovich, L. N., Lowell, R. P., & Ramondenc, P. (2011). Magmatic origin of hydrothermal response to earthquake swarms: Constraints from heat flow and geochemical data. *Journal of Geophysical Research*, *116*, B05103. https://doi.org/10.1029/2009JB006588

Ghosal, D., Singh, S. C., & Martin, J. (2014). Shallow subsurface morphotectonics of the NW Sumatra subduction system using an integrated seismic imaging technique. *Geophysical Journal International*, *198*(3), 1818–1831. https://doi.org/10.1093/gji/ggu182

Gillis, K. M. (2002). The rootzone of an ancient hydrothermal system exposed in the Troodos ophiolite, Cyprus. *The Journal of Geology*, *110*(1), 57–74. https://doi.org/10.1086/324205

Gillis, K. M., & Roberts, M. D. (1999). Cracking at the magma-hydrothermal transition: Evidence from the Troodos ophiolite, Cyprus. *Earth and Planetary Science Letters*, *169*(3-4), 227–244. https://doi.org/10.1016/S0012-821X(99)00087-4

Gomes, A., & Chazalnoel, N. (2017). Extending the reach of FWI with reflection data: Potential and challenges, 79th EAGE Conference and Exhibition, Paris, France (EarthDoc), https://doi.org/10.3997/2214%E2%80%934609.201701714.

Goss, A. R., Perfit, M. R., Ridley, W. I., Rubin, K. H., Kamenov, G. D., Soule, S. A., … Fornari, D. J. (2010). Geochemistry of lavas from the 2005–2006 eruption at the East Pacific Rise, 9°46′N–9°56′N: Implications for ridge crest plumbing and decadal changes in magma chamber compositions. *Geochemistry, Geophysics, Geosystems*, *11*, Q05T09. https://doi.org/10.1029/2009GC002977

Hannington, M. D., Petersen, S., Herzig, P. M., & Jonasson, I. R. (2004). A global database of seafloor hydrothermal systems, including a digital database of geochemical analyses of seafloor polymetallic sulfides, *Geol. Surv. of Can*. Open File, 4598, 12.

Harding, A., Kent, G., Blackman, D., Singh, S., & Canales, J. P. (2007). A new method for MCS refraction data analysis of the uppermost section at a mid-Atlantic ridge core complex. *Eos, Transactions of the American Geophysical Union*, *88*, Fall Meet. Suppl., Abstract S12A-03.

Hasenclever, J., Theissen-Krah, S., Rüpke, L. H., Morgan, J. P., Iyer, K., Petersen, S., & Devey, C. W. (2014). Hybrid shallow on-axis and deep off-axis hydrothermal circulation at fast-spreading ridges. *Nature*, *508*(7497), 508–512. https://doi.org/10.1038/nature13174

Haymon, R. M., & White, S. M. (2004). Fine-scale segmentation of volcanic/hydrothermal systems along fast-spreading ridge crests. *Earth and Planetary Science Letters*, *226*(3-4), 367–382. https://doi.org/10.1016/j.epsl.2004.08.002

Haymon, R. M., Fornari, D. J., Edwards, M. H., Carbotte, S., Wright, D., & Macdonald, K. C. (1991). Hydrothermal vent distribution along the East Pacific rise crest (9°09′-9°54′N) and its relationship to magmatic and tectonic processes on fast spreading mid-ocean ridges. *Earth and Planetary Science Letters*, *104*(2-4), 513–534. https://doi.org/10.1016/0012-821X(91)90226-8

Haymon, R. M., Fornari, D. J., Von Damm, K. L., Lilley, M. D., Perfit, M. R., Edmond, J. M., … Olson, E. (1993). Volcanic eruption of the mid-ocean ridge along the East Pacific Rise crest at 9°45-52′N: Direct submersible observations of seafloor phenomena associated with an eruption event in April, 1991. *Earth and Planetary Science Letters*, *119*(1-2), 85–101. https://doi.org/10.1016/0012-821X(93)90008-W

Henig, A. S., Blackman, D. K., Harding, A. J., Canales, J. P., & Kent, G. M. (2012). Downward continued multichannel seismic refraction analysis of Atlantis massif oceanic core complex, 30N, mid-Atlantic ridge. *Geochemistry, Geophysics, Geosystems*, *13*, Q0AG07. https://doi.org/10.1029/2012GC004059

Herron, T. J., Ludwig, W. J., Stoffa, P. L., Kan, T. K., & Buhl, P. (1978). Structure of the East Pacific Rise crest from multichannel seismic reflection data. *Journal of Geophysical Research*, *83*(B2), 798–804. https://doi.org/10.1029/JB083iB02p00798

Herron, T. J., Stoffa, P. L., & Buhl, P. (1980). Magma chamber and mantle reflections—East Pacific Rise. *Geophysical Research Letters*, *7*(11), 989–992. https://doi.org/10.1029/GL007i011p00989

Hooft, E. E. E., Detrick, R. S., & Kent, G. M. (1997). Seismic structure and indicators of magma budget along the southern East Pacific Rise. *Journal of Geophysical Research*, *102*(B12), 27,319–27,340. https://doi.org/10.1029/97JB02349

Jacobs, A., Harding, A. J., & Kent, G. M. (2007). Axial crustal structure of the Lau back-arc basin from velocity modeling of multichannel seismic data. *Earth and Planetary Science Letters*, *259*, 239–255.

Johnson, H. P., Becker, K., & Von Herzen, R. (1993). Near-axis heat flow measurements on the northern Juan de Fuca ridge: Implications for fluid circulation in oceanic crust. *Geophysical Research Letters*, *20*(17), 1875–1878. https://doi.org/10.1029/93GL00734

Kelley, D. S., Baross, J. A., & Delaney, J. R. (2002). Volcanoes, fluids, and life at Mid-Ocean ridge spreading centers. *Annual Review of Earth and Planetary Sciences*, *30*(1), 385–491. https://doi.org/10.1146/annurev.earth.30.091201.141331

Kent, G. M., Harding, A. J., & Orcutt, J. A. (1993). Distribution of magma beneath the East Pacific rise between the Clipperton transform and the 9°17′N Deval from forward modeling of common depth point data. *Journal of Geophysical Research*, *98*(B8), 13,945–13,969. https://doi.org/10.1029/93JB00705

Lailly, P. (1983). The seismic inverse problem as a sequence of before stack migrations: Conference on inverse scattering, theory and application, *Society for Industrial and Applied Mathematics*, Expanded Abstracts, 206–220.

Langmuir, C. H., Bender, J. F., & Batiza, R. (1986). Petrological and tectonic segmentation of the East Pacific Rise, 5°30′-14°30′N. *Nature*, *322*(6078), 422–429. https://doi.org/10.1038/322422a0

Levander, A. R. (1988). Fourth-order finite-difference P-SV seismograms. *Geophysics*, *53*(11), 1425–1436. https://doi.org/10.1190/1.1442422

Lister, C. R. B. (1977). Qualitative models of spreading center processes, including hydrothermal penetration. *Tectonophysics*, *37*(1-3), 203–218. https://doi.org/10.1016/0040-1951(77)90048-8

Liu, L., & Lowell, R. P. (2009). Models of hydrothermal heat output from a convecting, crystallizing, replenished magma chamber beneath an oceanic spreading center. *Journal of Geophysical Research*, *114*, B02102.

Lowell, R. P., & Burnell, D. K. (1991). A numerical model for magma hydrothermal boundary layer heat transfer in the oceanic crust. *Earth and Planetary Science Letters*, *104*(1), 59–69. https://doi.org/10.1016/0012-821X(91)90237-C

Lowell, R. P., & Germanovich, L. N. (1994). On the temporal evolution of high-temperature hydrothermal systems at ocean ridge crests. *Journal of Geophysical Research*, *99*(B1), 565–575. https://doi.org/10.1029/93JB02568

Lowell, R. P., & Germanovich, L. N. (2004). Hydrothermal processes at mid-Ocean ridges: Results from scale analysis and single-pass models. In C. R. German, J. Lin, & L. M. Parson (Eds.), *Mid-Ocean ridges hydrothermal interactions between the lithosphere and oceans*, *Geophysical Monograph Series*, (Vol. 148, pp. 219–244). Washington, DC: American Geophysical Union.

Lowell, R. P., & Yao, Y. (2002). Anhydrite precipitation and the extent of hydrothermal recharge zones at ocean ridge crests. *Journal of Geophysical Research*, *107*(B9), 2183.https://doi.org/10.1029/2001JB001289

Lowell, R. P., Rona, P. A., & Von Herzen, R. P. (1995). Seafloor hydrothermal systems. *Journal of Geophysical Research*, *100*(B1), 327–352. https://doi.org/10.1029/94JB02222

Lowell, R. P., Farough, A., Hoover, J., & Cummings, K. (2013). Characteristics of magma-driven hydrothermal systems at oceanic spreading centers. *Geochemistry, Geophysics, Geosystems*, *14*(6), 1756–1770. https://doi.org/10.1002/ggge.20109

Luo, Y., & Schuster, G. T. (1991). Wave-equation traveltime inversion. *Geophysics*, *56*(5), 645–653. https://doi.org/10.1190/1.1443081

Lutz, R. A., Shank, T. M., Luther, G. W. III, Vetriani, C., Tolstoy, M., Nuzzio, D. B., … Reed, A. J. (2008). Interrelationships between vent fluid chemistry, temperature, seismic activity and biological community structure at a mussel-dominated, deep-sea hydrothermal vent along the East Pacific Rise. *Journal of Shellfish Research*, *27*(1), 177–190. https://doi.org/10.2983/0730-8000(2008)27%5B177:IBVFCT%5D2.0.CO;2

Macdonald, K. C., Fox, P. J., Perram, L. J., Eisen, M. F., Haymon, R. M., Miller, S. P., … Shor, A. N. (1988). A new view of the mid-ocean ridge from the behaviour of ridge axis discontinuities. *Nature*, *335*(6187), 217–225. https://doi.org/10.1038/335217a0

Macdonald, K. C., Fox, P. J., Miller, S., Carbotte, S., Edwards, M. H., Eisen, M., … Wilson, D. (1992). The East Pacific Rise and its flanks 8-18°N: History of segmentation, propagation and spreading direction based on seaMARC II and sea beam studies. *Marine Geophysical Research*, *14*(4), 299–344. https://doi.org/10.1007/BF01203621

MacLeod, C. J., & Yaouancq, G. (2000). A fossil melt lens in the Oman ophiolite: Implications for magma chamber processes at fast spreading ridges. *Earth and Planetary Science Letters*, *176*(3-4), 357–373. https://doi.org/10.1016/S0012-821X(00)00020-0

Marjanović, M., Carbotte, S. M., Carton, H., Nedimović, M. R., Mutter, J. C., & Canales, J. P. (2014). A multi-sill magma plumbing system beneath the axis of the East Pacific Rise. *Nature Geoscience*, *7*(11), 825–829. https://doi.org/10.1038/ngeo2272

Marjanović, M., Carton, H. D., Nedimović, M. R., Carbotte, S. M., Mutter, J. C., & Canales, J. P. (2015). Distribution of melt along the East Pacific Rise from 9°30′ to 10°N from an amplitude variation with angle of incidence (AVA) technique. *Geophysical Journal International*, *203*(1), 1–21. https://doi.org/10.1093/gji/ggv251

Menard, H. W. (1960). The East Pacific Rise. *Science*, *132*(3441), 1737–1746. https://doi.org/10.1126/science.132.3441.1737

Mora, P. R. (1987). Nonlinear two-dimensional elastic inversion of multi-offset seismic data. *Geophysics*, *52*(9), 1211–1228. https://doi.org/10.1190/1.1442384

Mutter, J. C., Carbotte, S. M., Nedimović, M. R., Canales, J. P., & Carton, H. D. (2009). Seismic imaging in three dimensions on the East Pacific Rise. *Eos, Transactions of the American Geophysical Union*, *90*, 374–375. https://doi.org/10.1029/2009EO420002

Newman, K., Nedimović, M., Delescluse, M., Menke, W., Canales, J. P., Carbotte, S. M., … Mutter, J. (2010). East Pacific Rise axial structure from a joint tomographic inversion of traveltimes picked on downward continued and standard shot gathers collected by 3-D MCS surveying. *Geophysical Research Abstracts*, *12*. EGU2010-13383, EGU General Assembly 2010

Nicolas, A., & Boudier, F. (1991). Rooting of the sheeted dike complex in the Oman ophiolite. In T. Peters, A. Nicolas, & R. G. Coleman (Eds.), *Ophiolite Genesis and Evolution of the Oceanic Lithosphere*, (pp. 39–54). Dordrecht, Netherlands: Kluwer Acad. https://doi.org/10.1007/978-94-011-3358-6_4

Nicolas, A., & Boudier, F. (2011). Structure and dynamics of ridge axial melt lenses in the Oman ophiolite. *Journal of Geophysical Research*, *116*, B03103. https://doi.org/10.1029/2010JB007934

Nicolas, A., Boudier, F., Koepke, J., France, L., Ildefonse, B., & Mevel, C. (2008). Root zone of the sheeted dike complex in the Oman ophiolite. *Geochemistry, Geophysics, Geosystems*, *9*, Q05001. https://doi.org/10.1029/2007GC001918

Nooner, S. L., Webb, S. C., Buck, W. R., & Cormier, M.-H. (2014). Post eruption inflation of the East Pacific Rise at 9°50′ N. *Geochemistry, Geophysics, Geosystems*, *15*(6), 2676–2688. https://doi.org/10.1002/2014GC005389

Orcutt, J. A., Kennett, B. L. N., & Dorman, L. M. (1976). Structure of the East Pacific Rise from an ocean bottom seismometer survey. *Geophysical Journal of the Royal Astronomical Society*, *45*(2), 305–320. https://doi.org/10.1111/j.1365-246X.1976.tb00328.x

Pedersen, R. B. (1986). The nature and significance of magma chamber margins in ophiolites: Examples from the Norwegian Caledonides. *Earth and Planetary Science Letters*, *77*(1), 100–112. https://doi.org/10.1016/0012-821X(86)90136-6

Pica, A., Diet, J. P., & Tarantola, A. (1990). Nonlinear inversion of seismic reflection data in a laterally invariant medium. *Geophysics*, *55*(3), 284–292. https://doi.org/10.1190/1.1442836

Pratt, R. G., & Goulty, N. R. (1991). Combining wave-equation imaging with traveltime tomography to form high-resolution images from crosshole data. *Geophysics*, *56*(2), 208–224. https://doi.org/10.1190/1.1443033

Ribando, R. J., Torrance, K. E., & Turcotte, D. L. (1976). Numerical models for hydrothermal circulation in the oceanic crust. *Journal of Geophysical Research*, *81*(17), 3007–3012. https://doi.org/10.1029/JB081i017p03007

Rona, P. A., & Tivett, D. A. (1992). Discrete and diffuse heat transfer at ASHES vent field, Axial volcano, Juan de Fuca ridge. *Earth and Planetary Science Letters*, *109*(1-2), 57–71. https://doi.org/10.1016/0012-821X(92)90074-6

Rosenberg, N. D., Spera, F. J., & Haymon, R. M. (1993). The relationship between flow and permeability field seafloor hydrothermal system. *Earth and Planetary Science Letters*, *116*(1-4), 135–153. https://doi.org/10.1016/0012-821X(93)90050-J

Rubin, K. H., Macdougall, J. D., & Perfit, M. R. (1994). ^{210}Po/^{210}Pb dating of recent volcanic eruptions on the sea floor. *Nature*, *368*(6474), 841–844. https://doi.org/10.1038/368841a0

Ryan, W. B. F., Carbotte, S. M., Coplan, J. O., O'Hara, S., Melkonian, A., Arko, R., … Zemsky, R. (2009). Global multi-resolution topography synthesis. *Geochemistry, Geophysics, Geosystems*, *10*, Q03014. https://doi.org/10.1029/2008GC002332

Sargent, C., Hobbs, R. W., & Gröcke, D. R. (2011). Improving the interpretability of air-gun seismic reflection data using deterministic filters: A case history from offshore cape Leeuwin, southwest Australia. *Geophysics*, *76*, B113–B125. https://doi.org/10.1190/1.3554396

Scheirer, D. S., Shank, T. M., & Fornari, D. J. (2006). Temperature variations at diffuse and focused flow hydrothermal vent sites along the northern East Pacific Rise. *Geochemistry, Geophysics, Geosystems*, *7*(3), Q03002. https://doi.org/10.1029/2005GC001094

Schoofs, S., & Hansen, U. (2000). Depletion of a brine layer at the base of ridge-crest hydrothermal system. *Earth and Planetary Science Letters*, *180*(3-4), 341–353. https://doi.org/10.1016/S0012-821X(00)00184-9

Schultz, A., Delaney, J. M., & McDuff, R. E. (1992). On the partitioning of heat flux between diffuse and point source venting. *Journal of Geophysical Research*, *97*(B9), 12,229–12,314. https://doi.org/10.1029/92JB00889

Sempere, J.-C., & Macdonald, K. C. (1986). Deep-tow studies of the overlapping spreading centers at 9°03′N on the East Pacific Rise. *Tectonics*, *5*(6), 881–900. https://doi.org/10.1029/TC005i006p00881

Shank, T. M., Fornari, D. J., Von Damm, K. L., Lilley, M. D., Haymon, R. M., & Lutz, R. A. (1998). Temporal and spatial patterns of biological community development at nascent deep-sea hydrothermal vents (9°50′N, East Pacific Rise). *Deep-Sea Research Part II*, *45*(1-3), 465–515. https://doi.org/10.1016/S0967-0645(97)00089-1

Shipp, R. M., & Singh, S. C. (2002). Two-dimensional full wavefield inversion of wide-aperture marine seismic streamer data. *Geophysical Journal International*, *151*(2), 325–344. https://doi.org/10.1046/j.1365-246X.2002.01645.x

Shtivelman, V., & Canning, A. (1988). Datum correction by wave-equation extrapolation. *Geophysics*, *53*(10), 1311–1322. https://doi.org/10.1190/1.1442409

Singh, S. C., Kent, G. M., Collier, J. S., Harding, A. J., & Orcutt, J. A. (1998). Melt to mush variations in crustal magma properties along the ridge crest at the southern East Pacific Rise. *Nature*, *394*(6696), 874–878. https://doi.org/10.1038/29740

Singh, S. C., Collier, J. S., Harding, A. J., Kent, G. M., & Orcutt, J. A. (1999). Seismic evidence for a hydrothermal layer above the solid roof of the axial magma chamber at the southern East Pacific Rise. *Geology*, *27*(3), 219–222. https://doi.org/10.1130/0091-7613(1999)027%3C0219:SEFAHL%3E2.3.CO;2

Sohn, R. A., Fornari, D. J., Von Damm, K. L., Hildebrand, J. A., & Webb, S. C. (1998). Seismic and hydrothermal evidence for a cracking event on the East Pacific Rise crest at 9500N. *Nature*, *396*(6707), 159–161. https://doi.org/10.1038/24146

Sohn, R. A., Hildebrand, J. A., & Webb, S. C. (1999). A microearthquake survey of the high temperature vent fields on the volcanically active East Pacific Rise (9°50′N). *Journal of Geophysical Research*, *104*(B11), 25,367–25,377. https://doi.org/10.1029/1999JB900263

Soule, S. A., Fornari, D. J., Perfit, M. R., & Rubin, K. (2007). New insights into mid-ocean ridge volcanic processes from the 2005–2006 eruption of the East Pacific Rise, 9°46′N–9°56′N. *Geology*, *35*, 1079–1082. https://doi.org/10.1130/G23924A.1

Soule, S. A., Escartín, J., & Fornari, D. J. (2009). A record of eruption and intrusion at a fast spreading ridge axis: Axial summit trough of the East Pacific Rise at 9–10N. *Geochemistry, Geophysics, Geosystems*, *10*, Q10T07. https://doi.org/10.1029/2008GC002354

Tarantola, A. (1984). Inversion of seismic reflection data in the acoustic approximation. *Geophysics*, *49*(8), 1259–1266. https://doi.org/10.1190/1.1441754

Tarantola, A. (1986). A strategy for nonlinear elastic inversion of seismic reflection data. *Geophysics*, *51*(10), 1893–1903. https://doi.org/10.1190/1.1442046

Tolstoy, M., Cowen, J. P., Baker, E. T., Fornari, D. J., Rubin, K. H., Shank, T. M., … Glazer, B. (2006). A sea-floor spreading event captured by seismometers. *Science*, *314*, 1920–1922. https://doi.org/10.1126/science.1133950

Tolstoy, M., Waldhauser, F., Bohnenstiehl, D. R., Weekly, R. T., & Kim, W.-Y. (2008). Seismic identification of along-axis hydrothermal flow on the East Pacific Rise. *Nature*, *415*, 181–184.

Toomey, D. R., Jousselin, D., Dunn, R. A., Wilcock, W. S. D., & Detrick, R. S. (2007). Skew of mantle upwelling beneath the East Pacific Rise governs segmentation. *Nature*, *446*(7134), 409–414. https://doi.org/10.1038/nature05679

Treister E., & Huber, E. (2016). Joint full waveform inversion guided by travel time tomography, 78th EAGE Conference and Exhibition, Vienna, Austria (EarthDoc) doi: https://doi.org/10.3997/2214%E2%80%934609.201601542.

Tromp, J., Tape, C., & Liu, Q. (2005). Seismic tomography, adjoint methods, time reversal and banana-doughnut kernels. *Geophysical Journal International*, *160*(1), 195–216.

Vasco, D., Peterson, J., & Majer, E. (1995). Beyond ray tomography: Wavepaths and Fresnel volumes. *Geophysics*, *60*(6), 1790–1804. https://doi.org/10.1190/1.1443912

Vera, E. E., Mutter, J. C., Buhl, P., Orcutt, J. A., Harding, A. J., Kappus, M. E., … Brocher, T. M. (1990). The structure of 0- to 0.2-m.y.-old oceanic crust at 9°N on the East Pacific Rise from expanded spread profiles. *Journal of Geophysical Research*, *95*(B10), 15,529–15,556. https://doi.org/10.1029/JB095iB10p15529

Virieux, J., & Operto, S. (2009). An overview of full-waveform inversion in exploration geophysics. *Geophysics*, *74*(6), WCC127–WCC152.

Von Damm, K. L. (2000). Chemistry of hydrothermal vent fluids from 9°–10° N, East Pacific Rise: "Time zero," the immediate posteruptive period. *Journal of Geophysical Research*, *105*, 11,203–11,222. https://doi.org/10.1029/1999JB900414

Von Damm, K. L. (2004). Evolution of the hydrothermal system at East Pacific Rise 9°50′N: Geochemical evidence for changes in the upper oceanic crust. In C. R. German, J. Lin, & L. M. Parson (Eds.), *Hydrothermal interactions between the lithosphere and oceans*, *Geophysical Monograph Series* (Vol. 148, pp. 285–305). Washington, DC: American Geophysical Union.

Von Damm, K. (2006). RESET06—AT15–6 a response cruise to a volcanic eruption at the Ridge2000 East Pacific Rise integrated study site, Cruise Report. Retrieved from http://www.marine-geo.org/link/data/field/Atlantis/AT15-06/docs/AT15-06_CRUISE_REPORT_RESET06.pdf

Von Damm, K. L., & Lilley, M. D. (2004). Diffuse flow hydrothermal fluids from 9°50′N East Pacific Rise: Origin, evolution, and biogeochemical controls. In W. S. Wilcock, et al. (Eds.), *The subseafloor biosphere at mid-Ocean ridges*, *Geophysical Monograph Series* (Vol. 144, pp. 245–268). Washington, DC: American Geophysical Union. https://doi.org/10.1029/144GM16

Waldhauser, F., & Tolstoy, M. (2011). Seismogenic structure and processes associated with magma inflation and hydrothermal circulation beneath the East Pacific Rise at 9°50′N. *Geochemistry, Geophysics, Geosystems*, *12*, Q08T10. https://doi.org/10.1029/2011GC003568

Wang, H., Singh, S. C., & Calandra, H. (2014). Integrated inversion using combined wave-equation tomography and full waveform inversion. *Geophysical Journal International*, *198*(1), 430–446. https://doi.org/10.1093/gji/ggu138

Weiss, M. C., Sousa, F. L., Mrnjavac, N., Neukirchen, S., Roettger, M., Nelson-Sathi, S., & Martin, W. F. (2016). The physiology and habitat of the last universal common ancestor. *Nature Microbiology*, *1*(9), 16116. https://doi.org/10.1038/nmicrobiol.2016.116

White, S. M., Haymon, R. M., Fornari, D. J., Perfit, M. R., & Macdonald, K. C. (2002). Correlation between volcanic and tectonic segmentation of fast-spreading ridges: Evidence from volcanic structures and lava flow morphology on the East Pacific Rise at 9°-10°N. *Journal of Geophysical Research*, *107*(B8), 2173. https://doi.org/10.1029/2001JB000571

White, S. M., Haymon, R. M., & Carbotte, S. (2006). A new view of ridge segmentation and near-axis volcanism at the East Pacific Rise, 8-12°N, from EM300 multibeam bathymetry. *Geochemistry, Geophysics, Geosystems*, *7*, Q12O05.

Wilcock, W. S. D. (1998). Cellular convection models of mid-ocean ridge hydrothermal circulation and the temperatures of black smoker fluids. *Journal of Geophysical Research*, *103*(B2), 2585–2596. https://doi.org/10.1029/97JB03252

Wilcock, W. S. D., & Delaney, J. R. (1996). The size of mid-ocean ridge sulfide deposits: Evidence for heat extraction from magma chambers or cracking fronts. *Earth and Planetary Science Letters*, *145*(1-4), 49–64. https://doi.org/10.1016/S0012-821X(96)00195-1

Wilcock, W. S. D., Tolstoy, M., Waldhauser, F., Garcia, C., Tan, Y. J., Bohnenstiehl, D. R., … Mann, M. E. (2016). Seismic constraints on caldera dynamics from the 2015 axial seamount eruption. *Science*, *354*(6318), 1395–1399. https://doi.org/10.1126/science.aah5563

Wilkens, R. H., Fryer, G. J., & Karsten, J. (1991). Evolution of porosity and seismic structure of upper oceanic crust: Importance of aspect ratios. *Journal of Geophysical Research*, *96*(B11), 17,981–17,995. https://doi.org/10.1029/91JB01454

Wilson, D. S., Teagle, D. A., Alt, J. C., Banerjee, N. R., Umino, S., Miyashita, S., … Ziegler, C. (2006). Drilling to gabbro in intact ocean crust. *Science*, *312*(5776), 1016–1020. https://doi.org/10.1126/science.1126090

Wolery, T. J., & Sleep, N. H. (1976). Hydrothermal circulation and geothermal flux at mid-ocean ridges. *Journal of Geophysical Research*, *84*, 249–275.

Woodward, M. J. (1992). Wave-equation tomography. *Geophysics*, *57*(1), 15–26. https://doi.org/10.1190/1.1443179

Xu, M., Canales, J. P., Carbotte, S. M., Carton, H., Nedimović, M. R., & Mutter, J. C. (2014). Variations in axial magma lens properties along the East Pacific Rise (9°30′–10°00′N) from swath 3-D seismic imaging and 1-D waveform inversion. *Journal of Geophysical Research: Solid Earth*, *119*, 2721–2744. https://doi.org/10.1002/2013JB010730

Yilmaz, O. (2001). Seismic data analysis, processing, inversion, and interpretation of seismic data. *Society of Exploration Geophysicists*.

Yuan, S., Fuji, N., Singh, S., & Borisov, D. (2017). Localized time-lapse elastic waveform inversion using wavefield injection and extrapolation: 2-D parametric studies. *Geophysical Journal International*, *209*(3), 1699–1717. https://doi.org/10.1093/gji/ggx118

Yücel, M., & Luther, G. W. III (2013). Temporal trends in vent fluid iron and sulfide chemistry following the 2005/2006 eruption at East Pacific Rise, 9 50°N. *Geochemistry, Geophysics, Geosystems*, *14*, 759–765. https://doi.org/10.1002/ggge.20088